ABSTRACT

Advanced Light Manipulation and Waveguiding in Plasmonic Nanostructured Optical Fibers

Indra Mani Ghimire, Ph.D.

Co-mentor: Howard Ho Wai Lee, Ph.D.
Co-mentor: Zhenrong Zhang, Ph.D.

Conventional optical fibers are well-known for their efficient light guiding mechanism. However, the dielectric properties of core and cladding materials (e.g.- doped silica and silica glasses) limit the functionality of the optical fibers. Therefore, the optical properties of the fibers, such as phase, polarization state, amplitude, mode profile are fixed and cannot be altered once after the fiber drawing fabrication. The advent of new fabrication technologies for optical nanostructures such as plasmonic and metasurfaces allows us to overcome these limitations by tailoring those optical properties for advanced light manipulation and the development of novel optical fiber devices.

In this dissertation, I have reported four main projects on integrating plasmonic and metasurface nanostructures into an optical fiber for novel optical functions. In the first project, I demonstrated in-fiber polarization-dependent color filters by nanopatterning asymmetric metallic metasurface array on the end-facet of polarization-dependent photonic-crystal fibers. The asymmetric cross-typed nanoslit metasurface arrays are fabricated on the core of the optical fiber using a focused ion beam milling technique.

Highly polarization- and wavelength-dependent transmission with transmission efficiency ~ 70 % in the telecommunication wavelength observed by launching light into two orthogonal linear polarization states of the fiber. In the second project, I have extended the use of the focused ion beam milling technique to fabricate Berry phase metasurfaces on conventional single-mode optical fiber. A focusing effect has been observed in these metasurface-optical fibers, leading to the development of in-fiber metalens.

The third project involves the integration of plasmonic nano-circuits on the facet of polarization-maintaining photonic crystal fiber (PM-PCF) and panda-shaped PM-optical fibers. A Yagi-Uda antenna-coupled low loss plasmonic slot waveguide is directly integrated on the optical fiber by direct milling technique. We demonstrated efficient coupling of light from the fiber core to the plasmonic slot waveguide. The light is then propagated in the plasmonic slot waveguide via the propagation of surface plasmon polaritons and emitted to the far-field in the output antenna located in the cladding. We further extend the design of the complex circuit by integrating multi-channels plasmonic waveguide with different waveguide lengths, polarization splitters, and optical directional coupler (ODC) onto the optical fiber. This project first proof-of-concept demonstration on developing an ultra-compact plasmonic network on the tip of optical fiber for advanced optical communications applications.

The final project consists of the study of optical modulation by incorporating vanadium dioxide (VO_2) nanocrystals into the air holes of anti-resonant hollow-core photonic crystal fibers (ARHCF). Efficient optical modulation is observed by inducing the insulator-to-metal phase transition of VO_2 at different temperatures.

Advanced Light Manipulation and Waveguiding in Plasmonic Nanostructured Optical Fibers

by

Indra Mani Ghimire, B.Sc., M.Sc.

A Dissertation

Approved by Department of Physics

____

Dwight P. Russell, Ph.D., Interim Chairperson

Submitted to the Graduate Faculty of
Baylor University in Partial Fulfillment of the
Requirements for the Degree
of

Doctor of Philosophy

Approved by the Dissertation Committee

____

Zhenrong Zhang, Ph.D., Chairperson

____

Howard Ho Wai Lee, Ph.D.

____

Jay Dittmann, Ph.D.

____

Gerald Cleaver, Ph.D.

____

Jonathan Hu, Ph.D.

Accepted by the Graduate School
May 2021

____

J. Larry Lyon, Ph.D., Dean

Page bearing signatures is kept on file in the Graduate School.

TABLE OF CONTENTS

LIST OF FIGURES

ACKNOWLEDGMENTS

First, I would like to thank Dr. Howard Ho Wai Lee and Dr. Zhenrong Zhang, my dissertation supervisors, for introducing me to this fascinating subject and for letting me participate in these projects. I am grateful to Dr. Lee for answering my questions patiently and answering my calls even in late nights and early mornings. His encouragement and support guided me to make progress.

I am also very grateful to my committee members Dr. Jay Dittmann, Dr. Gerald Cleaver, and Dr. Jonathan Hu for making themselves available despite their busy schedules. Also, I would like to express my gratitude to all my professors in the Physics department at Baylor and the staff in the office Marian Nunn Graves.

I owe a great debt of gratitude to my colleagues Sudip J. Gurung, who I have known since childhood, Khant Minn, Jingyi Yang, Quandong H., Md. Kazi Rokunuzzaman for working with me to help me understand some of the toughest concepts of physics and material science. I would like to take the time and thank our postdocs Satyendra Kumar Mishra, Oleksiy Anopchenko, Subhajit Bej in our research group (Lee's nano-photonics and plasmonic) for their helpful ideas while troubleshooting.

Also, I would like to remember my friends Dr.Suman Baral, Dr. Parashu Ram Nyaupane, Dr. Bao-Fei Li, and Prashanta G.C., and Dr. Meera Devi Gurung, my sisters Mamta, Muna, Narbada, and brother Milan Ghimire, and brothers in laws Bashu Dev Khanal and Kamal Basnet. A big Thank You to Waco Nepali Community for organizing cultural events that made me feel like Waco as a second home.

Finally, I would like to acknowledge Rina Khadka, my wife, for her endless love and undulating support.

DEDICATION

To my mom, specifically, who has traveled through all the difficult times during my childhood and both my parents for valuing the education most, which fruited to this level of higher education!

CHAPTER ONE

Introduction

1.1 Light Guiding in Optical Fiber

Optical fiber has been used extensively in telecommunication primarily because of its efficient light-guiding capacity. The light-guiding mechanism in the core of the optical fiber is attributed to the total internal reflection (TIR) phenomenon where light can be guided in the core glass with a higher refractive index compared with the cladding's refractive index, leading to low loss waveguiding for long-distance signal transmission (1). Traditionally, most commonly available single-mode optical fibers (e.g., SMF-28) are made of two solid glasses (core and cladding) with slightly different refractive indexes. There is another special kind of optical fiber, called photonic crystal fiber (PCF), made with single glass material with airy holes covering the cladding region along the fiber's length (2). The PCF provides unique possibilities to engineer the light-guiding properties through the arrangement of the holey structures. They have been used in various optical applications such as optical sensing (3, 4), Supercontinuum generation (5-7), gas-based non-linear optics studies (8, 9) to medical endoscopy (10, 11).

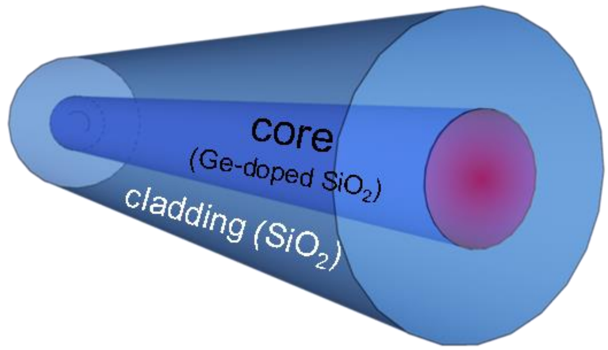

Fig. 1.1 Conventional optical fiber with core and cladding made with dielectric glasses.

The optical fibers are fabricated through well-developed fiber drawing technology. However, the optical properties of the optical fibers, such as phase, amplitude, polarization, cannot be altered after they are fabricated. Also, most of the optical fiber components (e.g., fiber-lens, fiber modulators) are bulky, expensive, and have limited functionality because of the material nature of glass. To modify optical properties and advance the optical fiber functionality, we use advanced nanophotonic structures, for instance, plasmonics and metasurfaces, and integrate them into the facet of the optical fibers for advanced light manipulation.

1.2 Surface Plasmon Polariton (SPP) Breaking the Diffraction Limit

The need for a smaller and compact device that operating with high operation speed is of utmost importance in this growing world of electronic devices. However, the size of these dielectric-based photonic devices is limited by the diffraction limit. For a medium with refractive index n, the diffraction limit is given by $d = \frac{\lambda}{2n}$, where $\boldsymbol{\lambda}$ is the wavelength of the incident radiation. This means that the size of the optical device cannot be made smaller than the diffraction limit. To break the diffraction limit in achieving optical guiding in sub-wavelength scale, surface plasmon polariton (SPP) comes as a promising solution. SPP is the oscillation of free electrons from the conduction band of metals as electromagnetic waves that travel along with the metal-dielectric interface with high optical bandwidth. They operate below the diffraction limit and are confined strongly to the metal surface (example in Fig. 1.2b).

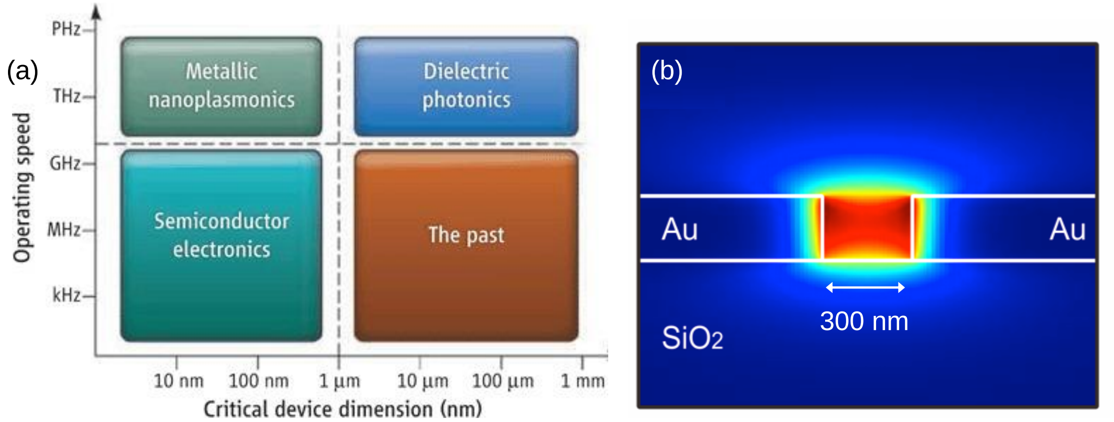

Fig. 1.2 (a) The limitations in operation speed and dimension of such optical devices for information technology. Dielectric photonics are comparatively large and are their size is limited by diffraction, hence the metallic nanoplasmonics comes into for a solution for future communication systems which constitutes photonics and electronics(12). (b) Example of plasmonic slot waveguide with confinement below the diffraction limit.

1.3 Metasurface for Wavefront Shaping

Metasurfaces are thin nanoscale resonator elements that allow the shaping of optical wavefront will be due to the light-matter interactions. These metallic/ dielectric elements resonantly couple with the electric/magnetic components of the electromagnetic field and perform properties that are not found in nature such as reflection, refraction, absorption, diffraction, etc. Due to the flat nature of metasurfaces (typical thickness < 100nm), they can enable novel ultrathin optical components such as flat lenses (13, 14), wave plates (15), holographic surfaces (16-20), and orbital angular momentum manipulation and detection devices (21-24) over a broad range of the electromagnetic.

1.4 Scope of the Thesis

In this study, we intend to merge three remarkable sciences, (i) highly confined plasmonic structures, (ii) optical metasurfaces, and (iii) optical fiber waveguides to develop novel optical functionality in optical fiber form (see Fig. 3). The objectives of our research are mainly to: -

1. Modify the optical properties of optical fibers by integrating plasmonic nanostructure and metasurface onto the end face of optical fiber.
2. Develop novel in-fiber plasmonic devices.
3. Demonstrate complex nanophotonic circuits on optical fiber.
4. Explore new optical properties and functionalities in optical fiber form.

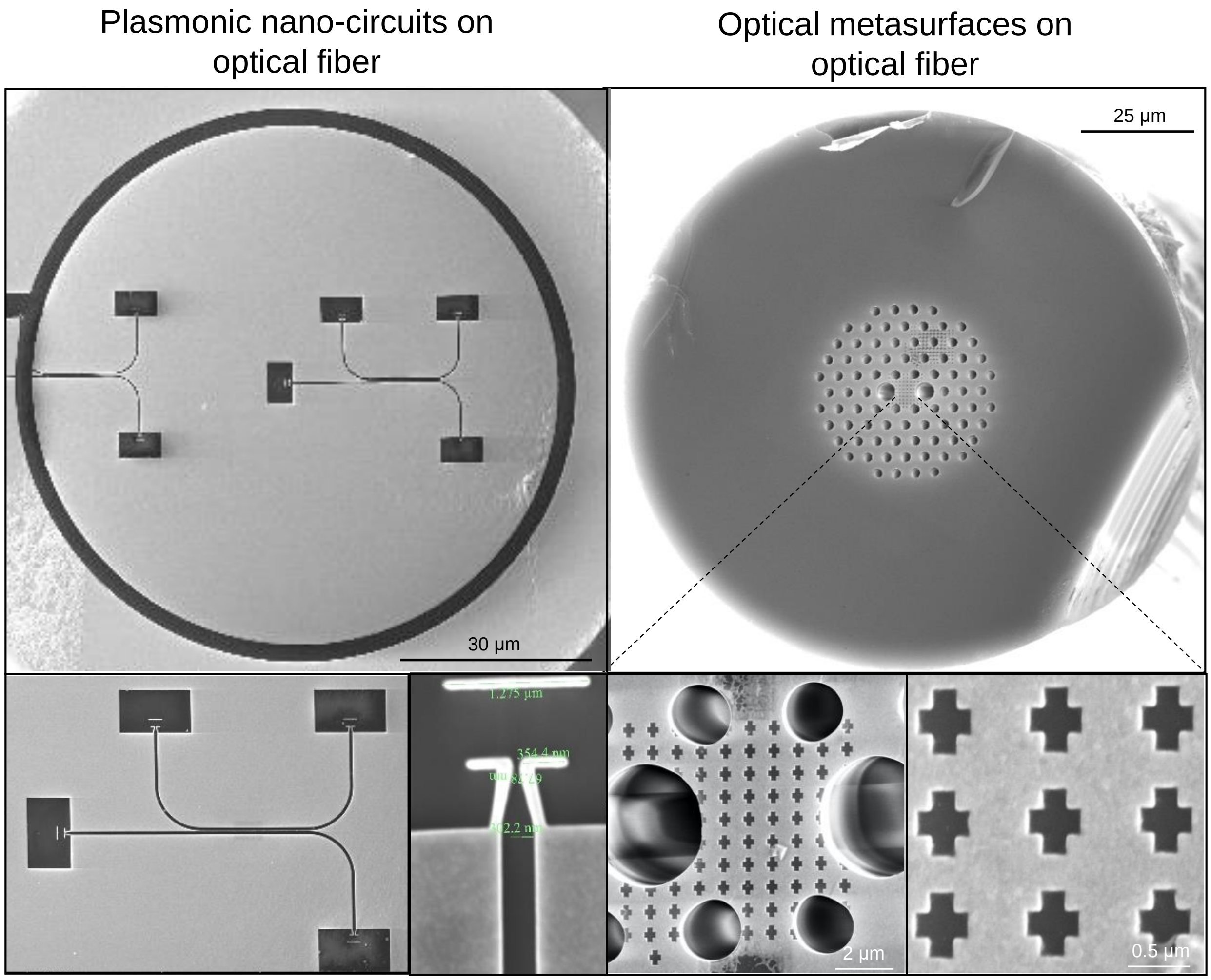

Fig. 1.3. Examples of integration of plasmonics and metasurfaces with optical fibers

1.5 Thesis Organization

Chapter two outlines the plasmonic slot waveguide assisted with a special kind of antenna, the Yagi-Uda antenna, which feeds the electromagnetic signal into the nanoscale channel of the plasmonic slot waveguide. This chapter consists of work led by myself (author) that explains the excitation of surface plasmon polaritons (SPP) that propagates through the waveguide channel between the interface of metal-dielectric media. The concept of a single plasmonic waveguide has been exploited to multiple of them to construct a complex network of nanocircuits. Multi-channels plasmonic waveguides, polarization splitting elements, and compact optical direction coupler have been demonstrated on optical fibers with advanced functionalities.

Chapter 3A discusses the utilization of metallic nano-slits and their orientation in different rotation angles for the design of fiber metalens using a geometric-phase antenna. The metalens in single-mode fiber (SMF) is fabricated using a focused ion beam (FIB) and the nano-slit antenna elements provide the required retarded phase which constituents to the focusing effect.This chapter is a part of published work led by one of my colleague. Chapter 3B discusses the design and realization of an ultracompact plasmonic color filter on the fiber tip. Here, the light-plasmon interaction with tiny periodic metallic cross nanoslits can be used to demonstrate the color filtering phenomenon.

Chapter Four discusses the experimental study of optical modulation of vanadium dioxide (VO_2) nanocrystal-filled antiresonant hollow-core photonic crystal fiber (ARHCF). The optical modulation is caused by the temperature-induced insulator-to-metal phase transition of vanadium dioxide (VO_2) nanocrystal.

Chapter five is the concluding chapter where the results obtained during the graduate study are summarized and stated.

CHAPTER TWO

2. Plasmonic Nano-circuit on Optical Fiber

This chapter in preparation as I Ghimire, K. Minn, B. Zechmann, H. W. Lee, “Integrated plasmonic nanocircuits on optical fibers,”to *Nature Photonics* (2021).

!

2.1 Introduction/ Motivation: Integrated Plasmonic Nano-circuits

With the electronic interconnects in complementary metal-oxide-semiconductor (CMOS) encounter a bottleneck on the intrinsic speed limit, interconnect density, and energy dissipation (1), alternative technologies such as optical nanocircuit are proposed to increase information processing speeds while reducing the size and energy consumption of communication devices. Optoelectronic components such as waveguides, light sources, modulators, have been integrated into the photonic integrated circuits (PIC) for sub-femtojoule signal processing and communication that could potentially overcome the electrical interconnects. However, there is a size mismatch between the nano-scale electronics and micron-scale photonics due to the diffraction limit of the dielectric photonic component in the PIC, thus ultracompact photonic nanocircuits are challenged to be realized.

In this context, plasmonics provides significant promise to bridge between electronics and photonics. Plasmonics offers light-guiding below the diffraction limit while still maintaining a high optical bandwidth, providing a different solution of nanoscale light wave processing (25),(26). The optical guided mode in the metal (plasmonic mode) can be guided and manipulated in the deep subwavelength scale that can provide an electrical and optical connection at the same time for PIC applications.

To form integrated plasmonic nanocircuits, numerous plasmonic components are demonstrated, and among them, plasmonic metal insulator metal (MIM) slot waveguide is one of the promising waveguide components since the light can guide and confine in nano-meter scale dimension (27). The plasmonic slot waveguide geometry has been used and demonstrated in various applications so far ranging from free space coupler (28), mode converters (29), resonator (30), photodetectors (31), directional couplers (32), and light sources (33).

It is indeed challenging to couple from free space into the plasmonic waveguides due to the nanoscale dimension of the plasmonic structures, hence a high numerical aperture (NA) lens is normally required (34). To achieve efficient coupling into subwavelength plasmonic waveguide mode from free space or optical fiber, several nano-couplers have been exploited such as plasmonic grating couplers (35).(36), plasmonic waveguide tapers (37),(38), nanoparticle coupler (39), and nanoantenna (40),(41). Out of these coupling structures, nanoantenna is one of the most convincing ways to concentrate light and convert the mode with high efficiency (42). A bow-tie antenna has shown 10% coupling efficiency when they were implemented as nano-couplers (43),(44). In a recent study by Kriesh *et.al*, the coupling in and out the efficiency of a special kind of nano-antenna, namely Yagi-Uda antenna, have shown 45% for in-coupling efficiency and 60 % of emission efficiency from the slot waveguide into the air and the substrate (32). In our work, we will utilize the Yagi-Uda antenna to assist the coupling into the plasmonic slot waveguides.

2.2 Integrating Plasmonic Nanocircuits on Optical Fibers:

The realization and functioning of these plasmonic nanocircuits in a planner substrate require sophisticated focusing optical systems to focus the light from long-distance communication channel (e.g., optical fiber) to highly focused spot to match with the sub-wavelength dimension of plasmonic waveguide with high efficiency. However, the optimized configuration will be direct coupling from optical fiber to plasmonic nano-circuit without using any bulky optical components. We aim to replace the chip-chip configuration and even fiber-chip configuration and move in a direction of combining these integrated circuits directly on the fiber end face. In this chapter, we develop a compact in-fiber device that consists of plasmonic nano-circuits on the fiber tip. These devices will potentially reduce the complexity of PIC and provide a stand-alone optical system that allows light coupling in and out of the nano-circuits for signal processing or sensing within the plasmonic nanocircuits. Such in-fiber nanocircuits will find applications in sensing, imaging, and optical communications. This proof-of-concept demonstration utilizes the fabrication technology in the fiber facet for a first-ever plasmonic network on the tip of optical fiber to exemplify how the patterning of the circuits can lead to the incorporation of compact optical circuits on fibers.

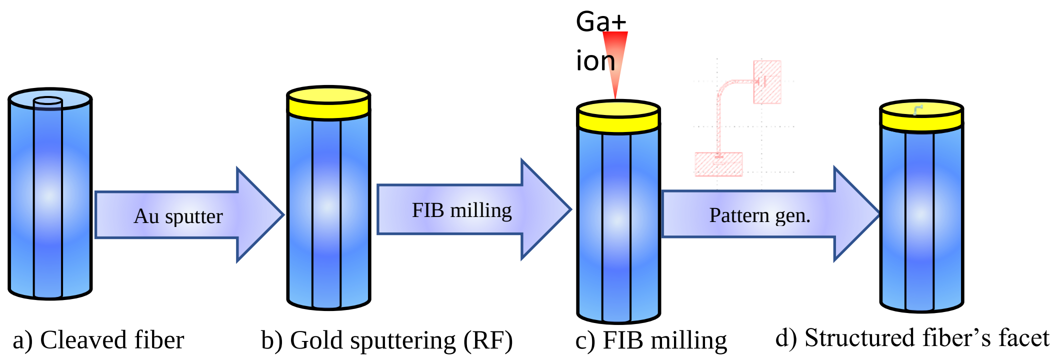

Fig. 2.1. Sample preparation on optical fibers.

Polarization-maintaining photonic crystal fibers (PCF) and panda-shaped (PS) optical fibers are used for these experiments. The end face is first cleaved, and a ~ 200 nm thick gold layer is deposited on the end face of the fiber via an RF magnetron sputtering machine with a chamber pressure of 10^{-3} torr. Such gold deposited fibers are then taken to the dual-beam focused ion beam scanning electron microscopy (FIB-SEM) for further processing - fabrication of the nanostructures. The Ga+ ion in the focused ion beam (FIB) is used to directly mill the nanostructures on the fiber. The fibers are attached to a holder vertically so that the tip of the fiber is as flat as possible along the cross-section. The applied voltage of 30 kV and ion beam current of 10 pA is used for the fabrication process. Special care is taken to make sure the fiber is not tilted and to allocate the fiber position in such a way that the center of the core of the fiber is correlated precisely with our designed pattern.

2.3 *Far-field Optical Measurement Setup*

We perform optical transmission measurements after the fiber samples are fabricated in the electron microscope. The optical measurement set-up is depicted in Figure2.2. A near-infrared laser (NIR) is launched using a single-mode fiber via an objective lens as a collimated light source. This laser is then directed using a mirror and an objective lens to focus down to the core of the structured fiber sample. The transmitted light from the fiber with plasmonic nanostructure in the output end is then collected using an optical spectrum analyzer (OSA) or recorded as images using a NIR camera. The collected images are further analyzed for their output and input intensities, and transmission is normalized with the bare fiber (without gold layer and nanostructures) with the same fiber length.

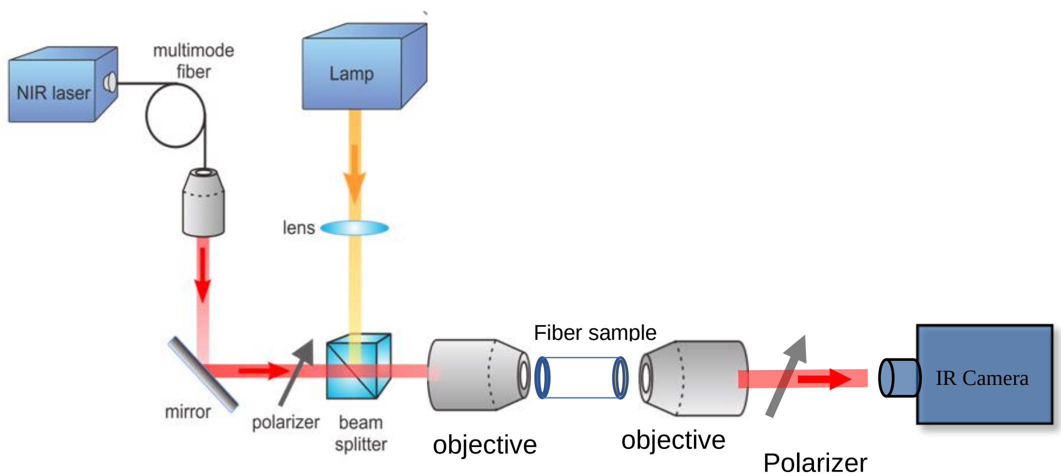

Fig. 2.2 Optical transmission measurement set-up.

Since the polarization state of incident radiation is a crucial factor in studying these structures, special caution is taken to align the input end of the sample fiber so that the polarization of the beam is aligned with the slow/fast optical axes of the fiber. This alignment can be done by using the camera to image the front face end of the fiber.

2.4 Yagi-Uda Antenna and the SPP Propagation

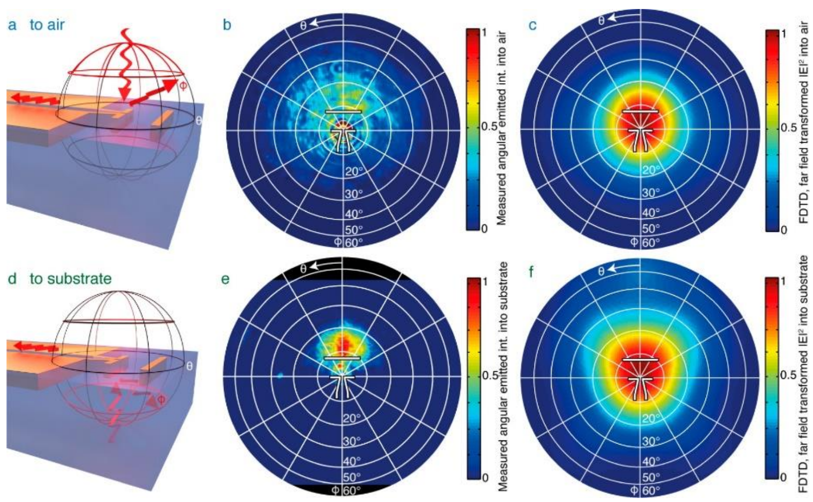

Fig 2.3. Emission directionality of Yagi Uda antenna: A narrow and strongly linear polarized angular emission directionality of the Yagi antenna at λ = 1550 nm (a–c) into the air and (d–f) into the silica substrate was measured experimentally by Fourier plane imaging of the antenna emission during excitation with (b) an objective of NA = 0.9 and (e) an immersion objective of NA = 1.3. The maximum azimuthal emission cone of 30° is following the 3D FDTD simulation of the same structure into (c) air and (f) silica.

Reference; A. Kriesh et.al “Functional plasmonic Nanocircuits with low insertion and propagation losses”, Nanoletters (2013).

Yagi-Uda type nanoantenna is used to couple the electromagnetic signal into the plasmonic slot waveguide and to achieve narrow directionality. The emission directionality is illustrated in detail in Fig.2.3 where angular dependence is shown in both the configuration a) to air and b) to substrate. This study is performed on the glass planner substrate and is from a journal published in ACS nano letters, referenced, a work by A. Kriesh *et.al*. The components of such an antenna consist of active and passive elements. It mainly contains the two-dipole antenna, and each of them is connected to the plasmonic waveguide slot via a feeding element. The passive element, the reflector, sits on the back of the dipole antenna which further enhances the feeding mechanism into the waveguide. The length of the antenna is so chosen that they have maximum coupling efficiency at 1550 nm.

2.5 Single Plasmonic Slot Waveguide on Optical Fiber

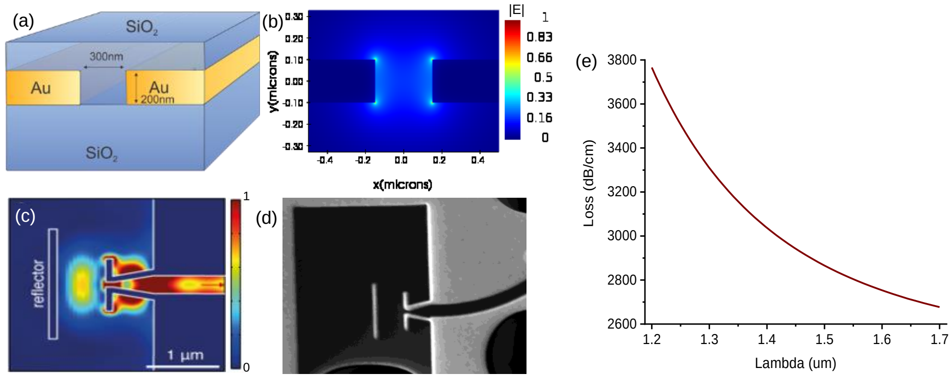

Fig. 2.4 (a) Schematic of single plasmonic slot waveguide. (b) Cross-section mode profile of the waveguide. (c) Simulated field distribution and (d) SEM image of the Yagi-Uda nanoantenna. (e) Simulated loss of the plasmonic waveguide with for a fundamental waveguide mode.

Our design of a single plasmonic waveguide (SWG) consists of a plasmonic slot waveguide assisted with the Yagi-Uda antenna in both input and output ends (Fig. 2.4). The feeding antenna couple electromagnetic wave (EM) to the surface plasmon polariton (SPP) guided mode in the plasmonic slot waveguide (Fig. 2.4b). Such guided waveguide mode is also called gap plasmon mode. Fig. 2.4a depicts the geometry of the plasmonic slot waveguide that has been exploited in our work. As shown in the mode profile in Fig. 2.4c, the optical field is highly localized in the slot waveguide with a dimension of 300 x 200 nm. The gap plasmon mode will then propagates along the waveguide and could be emitted to the far-field through the output antenna. The simulated optical loss of the fundamental plasmonic mode versus wavelength is shown in Fig. 2.4d. Propagation of loss of ~ 0.28 dB/μm at the wavelength of 1550 nm is observed which is relatively low loss compared with other plasmonic waveguides.

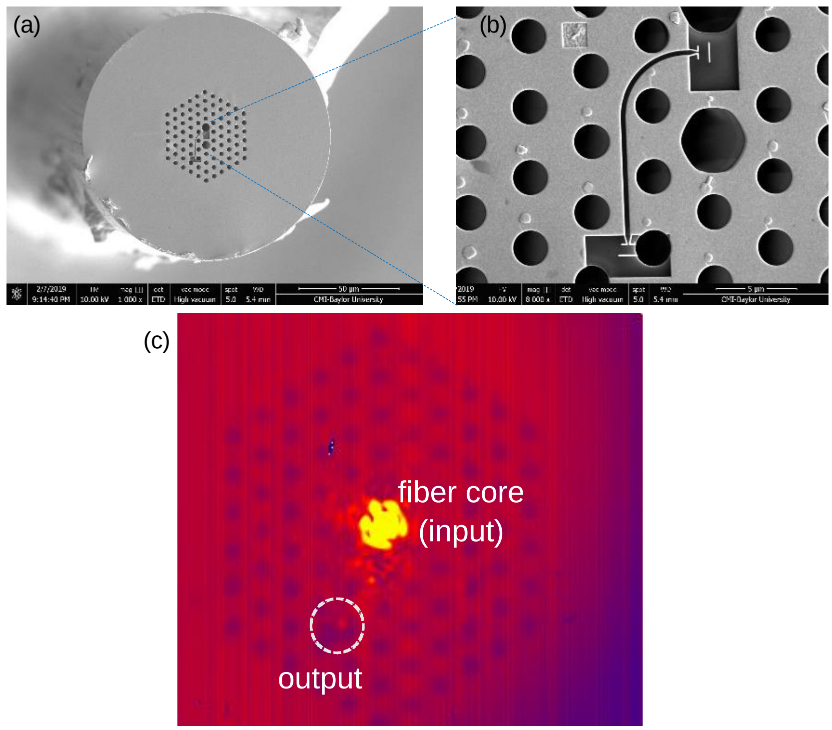

Fig. 2.5 (a) SEM image of the single plasmonic waveguide on PCF. (b) Zoom-in image of (a), (c) Far-field measurement image.

For our experimental realization, SWG is fabricated on a polarization-maintaining photonic crystal fiber (PM-PCF) sample. Figure 2.5a shows the SEM micrograph image of such SWG fabricated on the surface of the PM-PCF. The SWG originates from the core (core diameter of 5.8 μm) of the optical fiber and extends to the cladding region. A far-field measurement from the SWG in PCF sample fiber is shown in fig 2.5c. A bright light spot at the output region initially demonstrates the successful plasmonic coupling from/to the antenna and the SPP propagation in the slot waveguide.

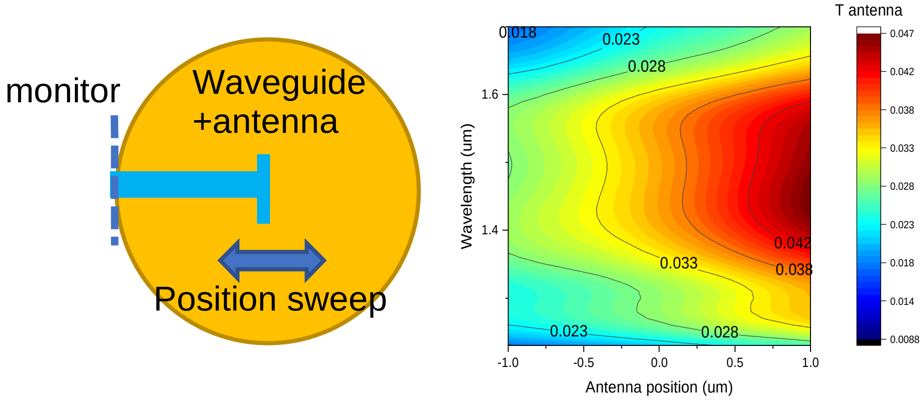

Fig. 2.6. Simulated transmission of light coupled from the core of optical fiber to the plasmonic slot waveguide with different horizontal antenna positions.

The functionalization and mechanism of an SWG are studied via full-wave numerical FDTD simulations. To understand the effect on the coupling efficiency with the position of the antenna within the core, we simulated the antenna structure with different vertical positions within the core. Figure 2.6 illustrates the impact of coupling intensity from the core to the slot waveguide with different horizontal offset positions for the input antenna from the center of the core of the optical fiber. Higher coupling is found when the antenna is located about 1 micrometer to the right side of the center of the core.

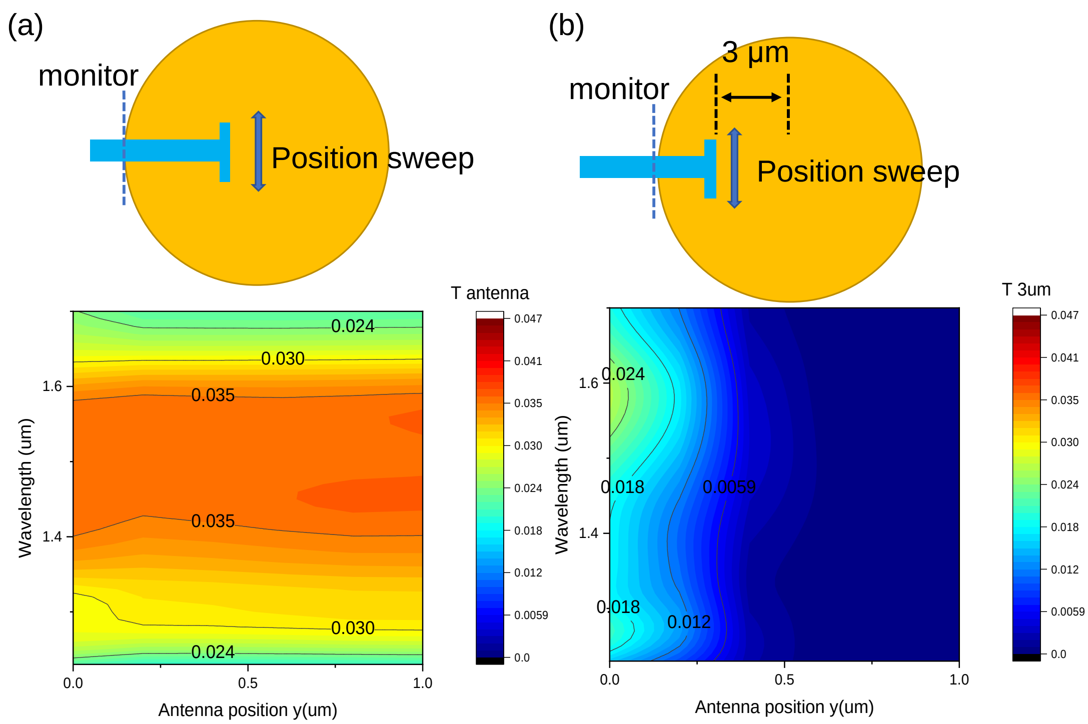

Fig. 2.7. Simulated transmission of light coupled from the core of optical fiber to the plasmonic slot waveguide with different horizontal antenna positions.

Figures 2.7 show the impact of the vertical offset of the antenna from the center of the core of the optical fiber. For the case with an antenna located in the center of the core (horizontally), the variation of the antenna vertical position does not show too much dependence (Fig. 2.7a). However, for the case with the antenna is shifted horizontally of 3 μm from the core, the optimal position to achieve the maximum power coupled to the cladding region is the exact center of the core, and an offset to the +y or -y direction gives a large loss difference as depicted by Fig. 2.7b. As an example, a vertical shift of 200 nm from the center results in a 50% loss in the power coupled to the waveguide.

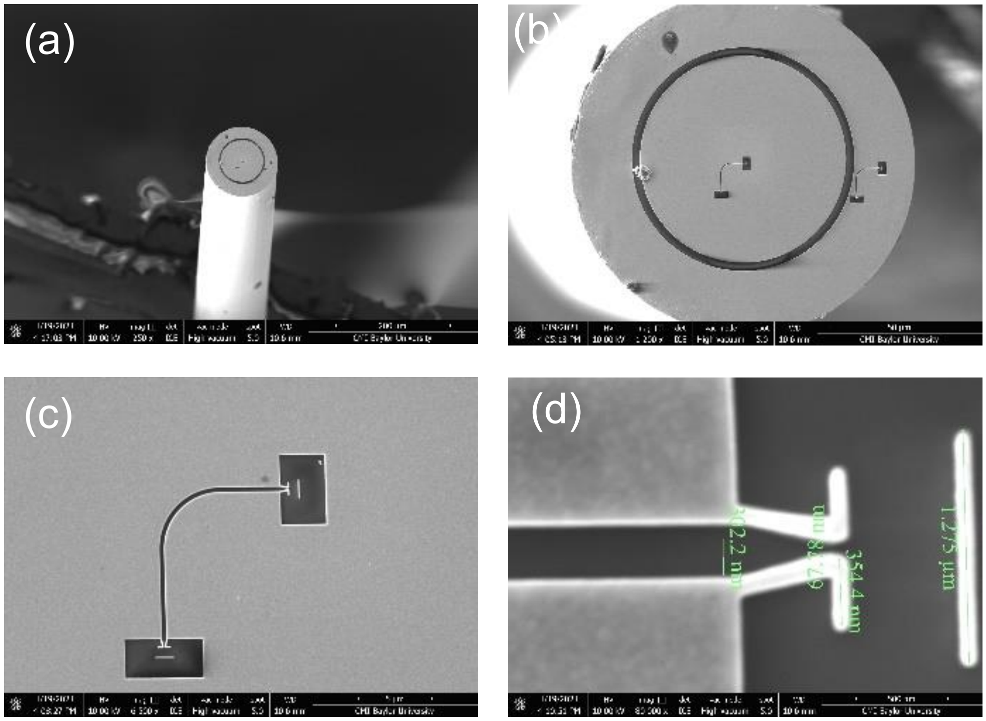

Fig. 2.8 SEM images (a) Unpattern fiber facet. (b) Polarization splitter patterned on the single-mode fiber: (c) and (d) Zoom-in image of the splitters.

Next, the structure is patterned on conventional panda-shaped polarization-maintaining optical fiber as shown in the SEM images in Figure 2.8. These fibers have two big lobes of higher refractive index material that surrounds the solid core on either side, although not visible in fig. 2.8b due to the ~200 nm thick gold layer deposited on top. The detail of the dimensionality of the fabricated Yagi-Uda antenna can be seen from Fig. 2.8d, where components of the SWG and antenna such as the gap between the two dipole antenna components and the width of the waveguide are close to our design of 80 nm and 300 nm, respectively. The sample is then measured with the far-field measurement setup. Measured optical images show the detection of a significant amount of emitted light from the output antenna, implying good coupling and propagation of the SPP in the slot waveguide (Fig. 2.9). Two NIR optical camera images for the incident lights at a wavelength of 1550 nm and 1630 nm are shown in Figs 2.9a and 2.9b. Figure 2.9a provides the overlapped optical image and SEM image of the structure which demonstrates the light is emitted from the output antenna at the cladding. The NIR images of the end facet are recorded at every 5 nm step size from 1500 -1630 nm. These images of the coupled output antenna are then normalized to that of a blank PS fiber of similar length with the same input laser power. This normalized data gives the coupling efficiency of the single waveguide at the wavelength range of 1500 -1630 nm as shown in fig 2.9d. The result shows the total efficiency for the SWG (including input/output coupling, bending loss, and propagating loss) is measured to be ~0.2% in the wavelength range of 1500 -1630 nm.

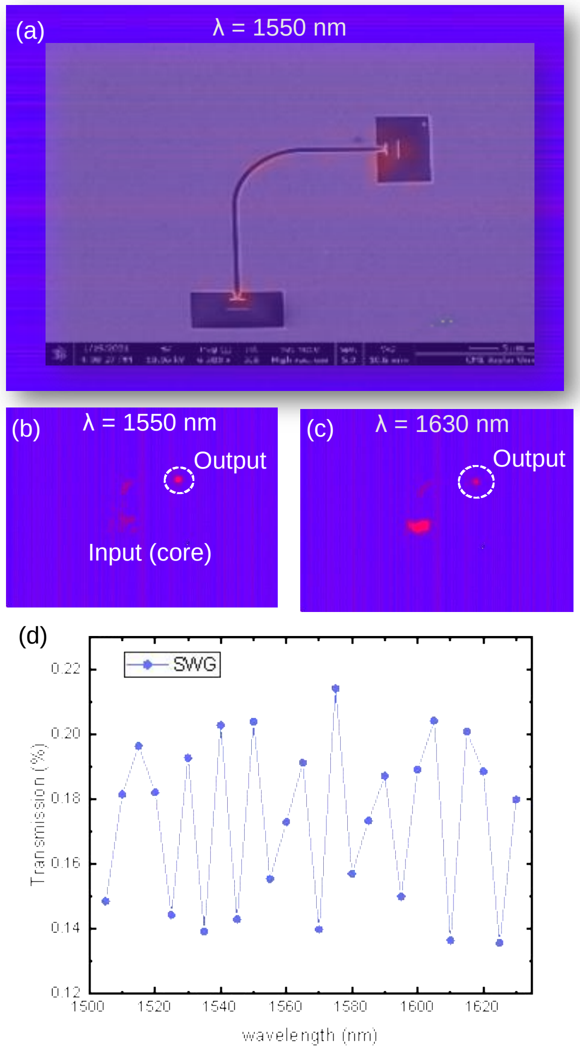

Fig. 2.9 Far-field optical measurement (a) Overlapped with SEM image at a wavelength of 1550 nm: without SEM image at a wavelength of (b) 1550 nm, and (c) 1630 nm (d) Total efficiency from the output antenna.

Since an SWG consists of mainly three components – input antenna, plasmonic slot waveguide, and output antenna, the total transmission from such SWG as a function of wavelength is given by,

$T_{tot}(\boldsymbol{\lambda}) = T_{ant}(\boldsymbol{\lambda})^2\ Twg\ (\boldsymbol{\lambda})$ ………………………….. (2.1)

Where $T_{ant}(\boldsymbol{\lambda}) = P_{wg}(\boldsymbol{\lambda}) / P_{freespace}(\boldsymbol{\lambda})$ represents w the spectral transmission of the antenna which is a ratio of how efficiently the antenna couple into the waveguide mode of the slot waveguide, and Twg ($\boldsymbol{\lambda}$) is the transmitting ability of the plasmonic slot waveguide. The total coupling efficiency from the single plasmonic waveguide structure with two input/output antenna in optical fiber is defined as

$$\eta = \frac{power\ emitted\ at\ the\ output\ antenna\ detected\ at\ cross\ pol.}{total\ power\ from\ the\ core\ of\ a\ blank\ fiber\ at\ parallel\ pol.} \times 100\ \%$$

2.6. Plasmonic Multi-channel Waveguide in PCF and PS Fiber

To extend the complexity and further study the plasmonic coupling in the optical fibers, four-channel plasmonic waveguides have been fabricated on optical fiber (Fig. 10). All the waveguides emerge from a rectangular opening on the core of the fiber and extend in the horizontal direction for about 4 microns and 90^0- bending part with 4 microns as the radius of curvature. After the bend, the waveguide is attached to a vertical waveguide and an output antenna at the end of the waveguide for emission into the far field. Each branch varies with 4-6 microns in waveguide's length so that the waveguide loss could be measured from the emission intensities of four different waveguides. Since the metallic slot waveguide is lossy, the longer waveguide is expected to dissipate more energy along its path. We anticipate the highest loss (dimmest output light) in the longest waveguide (waveguide 4) and the emission intensities should follow the order of waveguide 1,2,3, and 4. Our result shows the correct trend for waveguide 1, 2, 4 (e.g., $I_1 > I_2 > I_4$). However, disagreement is found when comparing with waveguide 3 (which is dimmest). We believe the disagreement on the order of the emission intensity of waveguide 3 might result from the distortion of field confinement from the cladding holes close to the antenna, remaining gold particles along the waveguide, or imperfect sidewall roughness for this waveguide. Further investigation is needed, and more experiments have been performed in standard optical fiber without the cladding holes as discussed in the following.

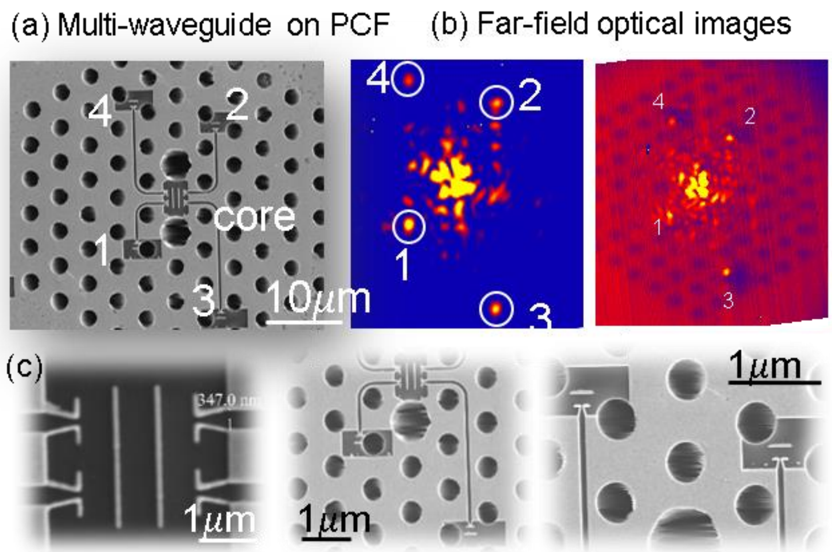

Fig.2.10 (a) SEM images of a Yagi-Uda antenna assisted multi-waveguide in PM- PCF fiber. (b) Far-field measurement at 1550 nm without/with background light. (c) Zoom-in image of 4-waveguides: input antenna at the core; output (bottom two and top two).

To obtain a larger flat platform for designing and fabricating a complex waveguide network, we fabricated multi-channel waveguides on the polarization-maintaining panda-shaped fiber which is a single-mode fiber. The use of this special single-mode fiber gives more degrees of freedom for the design of our structure as its geometry does not have to dodge the airy holes as in the case of PM-PCF. The optical measurements of the sample at a wavelength of 1550 nm are shown in Figure 2.11. The emission intensity from the four waveguides follows the distribution as we expected ($I_1 > I_2 > I_2 > I_4$). The intensities from the output spots for these four waveguides are collected and analyzed, and the results are shown in Fig. 2.11c. From Fig. 2.11c, we calculated the propagating loss of the plasmonic slot waveguides and found the value of 0.30 dB/μm at 1550 nm, which is close to the simulated loss of 0.28 dB/μm (Fig. 2.4e).

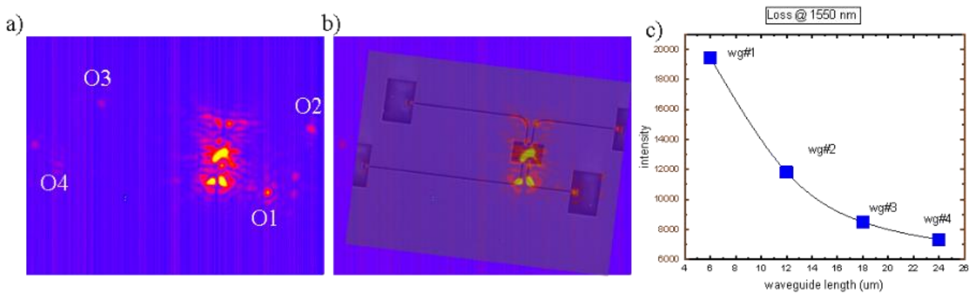

Fig. 2.11 (a) Far-field measurement at wavelength of 1550 nm from a Yagi-Uda antenna assisted Multi-waveguide (MWG) in PM-PS fiber. (b) far-field measurement at 1550 nm overlapped with SEM micrograph of MWG structure. (c) Emission intensity variation with waveguide's lengths at a wavelength of 1550 nm.

Even though the loss from MWG in PS fiber is observed with the length of the waveguide, the emission spot for the longest waveguide (waveguide 4) shows some splitting effect, which is currently still being investigated. To better understand the structure, we have tried to fabricate better quality of the MWG on the PM-PS fiber facet. Figure 2.12 depicts the SEM micrograph images of a newly fabricated MWG sample whose quality, sharpness of the slot waveguide's wall, and the dimension of the antenna are of the best quality obtained so far. The modification on the design of this structure is mostly on the lengths of the waveguide, bending radius of curvature to 4 μm. Each waveguide has a horizontal extended arm of 4 μm, tailored with a circular bend ($1/4^{th}$) of a circle, which gives a 90-degree bend. The waveguides have an additional length consists of vertical slot waveguide of 6 μm, 10 μm,18 μm, and 24 μm for the shortest to longest of them, respectively. The optical measurement from this sample (Fig.2.12) is still under investigation.

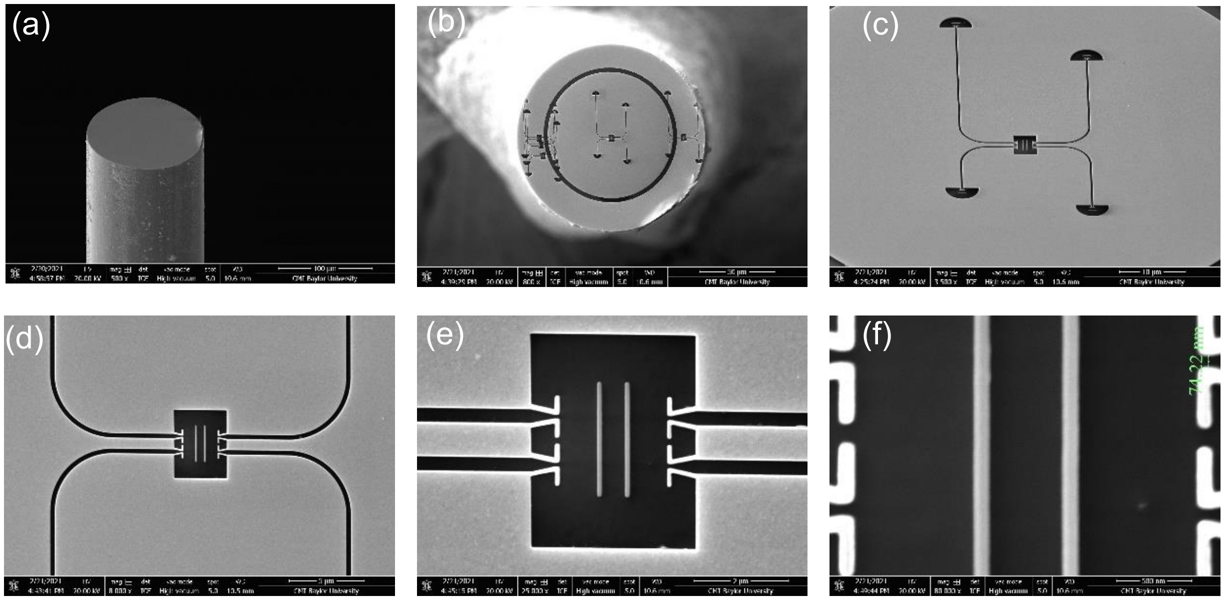

Fig. 2.12. (a) SEM images of a Yagi-Uda antenna-assisted multi-waveguide in PM- PCF fiber. (b) far-field measurement at 1550 nm without/with background light. (c) Zoom-in image of 4-waveguides: input antenna at the core; output (bottom two and top two).

2.7 Polarization Splitter (PS) in Fiber

The motivation behind the design of the polarization splitter is to switch the output signal of the nano-circuit on fiber with the polarization state of the core mode. In the optical measurement, an extra optical component, a half-wave plate, is added just after the linear polarizer at the input end. The half-wave plate is rotated in any direction to change the polarization state of the incident light that goes into the fiber. The use of this half-wave plate is important as it changes the polarization by 2ѳ when rotated with angle ѳ while offering almost zero effect on coupling/alignment in the optical path. For example, as shown in Fig.2.13, the horizontal polarization state of the incident signal in the fiber excites the input antennas that are aligned to the respective polarization and hence waveguide 1 (W3) and waveguide 4 (W4) are lighted up/ transmission is observed. Similarly, if the incident polarization is switched to vertical, the rest of the antenna pair (W2 and W3) are lighted up (as in Fig. 2.13d). If the light were incident at any other angles, then the transmission would be obtained as per their resolute component in each direction. Ideally, each of the four-output antennae should be observed to be equally emitting the signal when the incident polarization state is at 45^0 to the horizontal. For this measurement, we only employed the input linear polarizer and a half waveplate, and no output polarizer at the output end was used. The angular dependence of the input polarization state with the transmission intensities of such antenna at each angle from 0-90 degrees has been studied further, as in Fig. 2.13f. In this plot, the equal intensity spot is observed to be around 30 degrees which are slightly different than the expected angle of 45-degree. We have fabricated another best-quality sample fabrication to further investigate the polarization effects (Fig. 2.14). The polarization-resolved far-field measurements from the sample in Fig. 2.14 are currently under investigation.

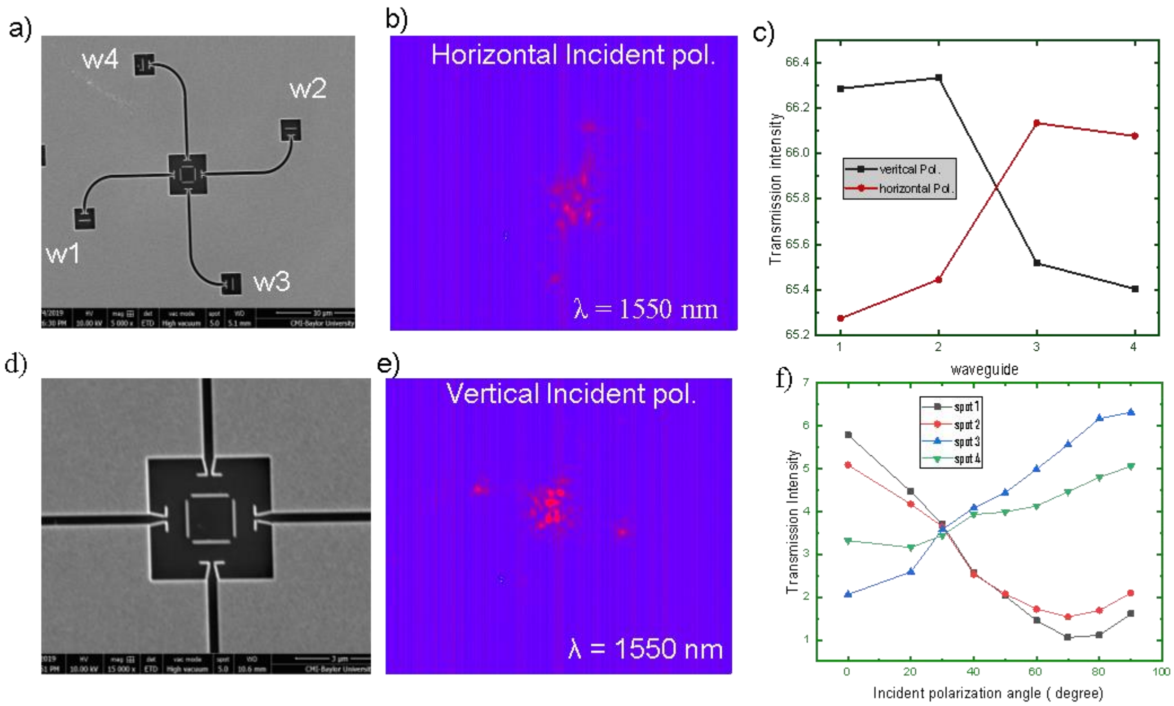

Fig. 2.13 (a) SEM image of four waveguides to illustrate polarization splitting fabricated on single-mode fiber. (b) Far-field measurement at a wavelength of 1550 nm with incident radiation horizontally polarized. (c) Intensity calculation from the far-field measurements for two orthogonal incident polarization detected at cross-polarization (d) Zoom-in image of the fabricated polarization splitter. (e) Far-field measurement at a wavelength of 1550 nm with incident radiation vertically polarized. (f) Intensity calculations from the far-field measurement for angular dependence of the incident light.

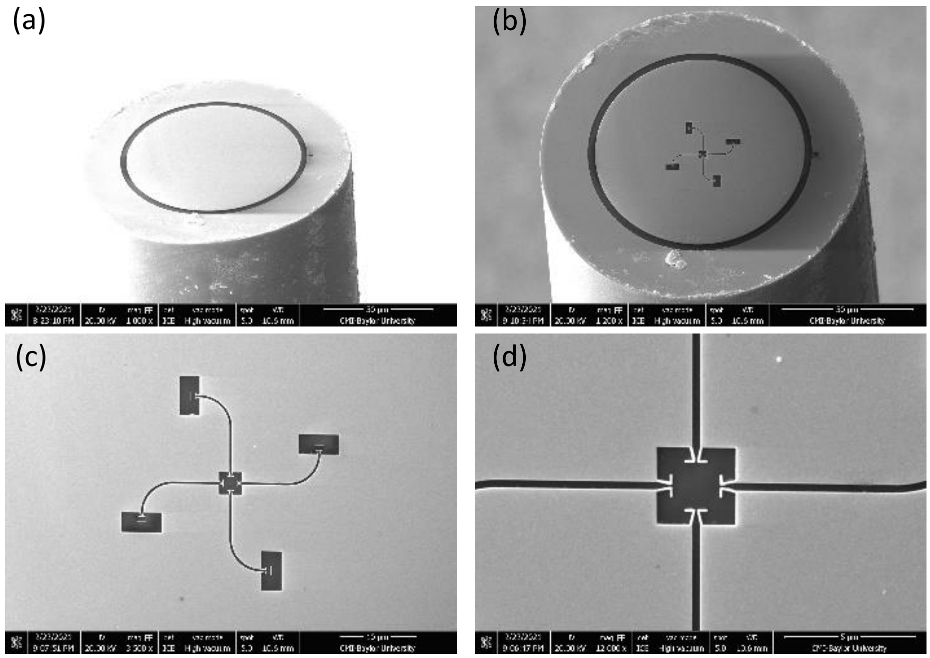

Fig. 2.14 SEM images of polarization splitter: (a) Unpattern fiber facet. (b) Polarization splitter patterned on the single mode fiber: (c) and (d) Zoom-in image of the splitters.

2.8 Plasmonic Optical Directional Coupler

This design of the Optical Directional Coupler (ODC) consists of a single waveguide structure and an additional waveguide that runs parallel to the horizontal section of it (Fig. 2.15a). The thickness of the thin metallic film that separates the two parallel running waveguides is in the range of 50 -100 nm. Several studies have been performed on this type of ODC structure on planar substrates where the power transfer is shown to take place between the adjacent waveguides due to the coupling of evanescent fields (32). We fabricated the plasmonic ODC structure directly on the end face of the fiber. The input antenna is located in the center of the core and the two probe antennas that used to detect the ratio of intensities at both the outputs are located in the cladding region. The incident polarization state of the incoming radiation is along with the input antenna orientation which helps to couple the SPP mode in the slot waveguide effectively as discussed before.

One probe antenna attached along the parent SWG is called bar antenna (the corresponding intensity of light, I_{bar} , also referred to output-ref as in Fig.2.15) whereas the other probe output that is attached to the coupling waveguide is called cross antenna (the corresponding intensity of light, I_{cross} , also referred as output-2 in Fig.2.15). Previous work by A.kriesh *et.al*, they showed that the ODC nano-circuitry gives the high dispersive feature with 30 dB over wavelength difference of 200 nm (32).

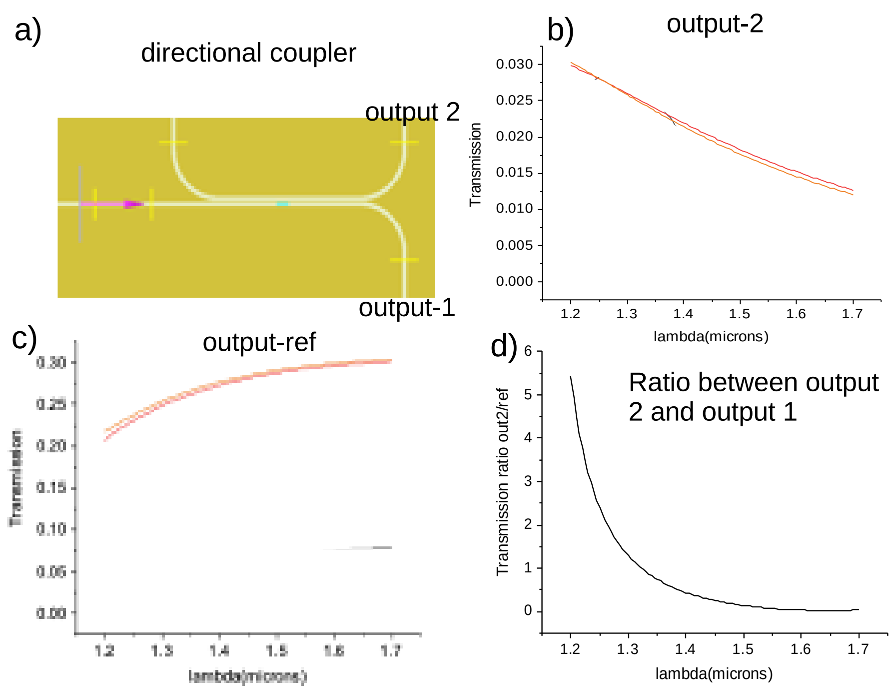

Fig. 2.15 FDTD simulation for optical directional coupler in single mode fiber. (a) schematic for ODC on optical fiber. Transmission at the (b) output-2 (c) output-1. (d) Transmission ratio between two outputs. The ratio shows the dispersive nature of the ODC.

A typical ODC circuit we have used for our research consists of an input Yagi-Uda antenna that is tailored by a single slot waveguide with a length of 22 µm (horizontal portion) and a 6 µm a vertical slot waveguide section connected to the output antenna. An additional slot waveguide that runs parallel to the wavelength from the input has a horizontal length of 10 µm where the coupling of the evanescent field is observed. Both ends of this new slot waveguide are tailored to the output antenna, after 90^0 bend and vertical waveguides. The output at the right end is called bar output. To understand the coupling between the waveguides on the ODC, we performed FDTD numerical simulation.

Figure 2.15 shows the FDTD simulation results. A guided mode is launched to the input end of the structure and the transmission intensity is monitored at the two branches – output-ref (the same parent SWG) and output-2 (the coupled slot waveguide). Figure 2.15d depicts the ratio between the two outputs, showing high directionality over 200- 300 nm spectral range. Thus, we will integrate the ODC plasmonic structure in PS optical fiber to investigate the coupling effect and to demonstrate a potential application for wavelength-dependent optical fiber switches and splitters.

We fabricated ODC in the facet of PS fiber and measured the far-field optical images. Figure 2.16a shows the SEM image of an ODC fabricated on the tip of PS fiber. The far-field measurements are performed for the wavelength range 1500-1630 nm at each 5nm step size. The optical image at a wavelength of 1500 nm shows the higher emission from O1(cross output) than O2 (bar output), while almost similar intensities are observed for both output O1 and O2 at a wavelength of 1550 nm, shown in Fig. 2.16b, c. At a wavelength of 1630 nm, the output O2 has a higher emission (Fig. 2.16d). A transmission ratio (cross/bar) is plotted in Fig. 2.16f for both the simulation result (black curve) and experimentally measured results (red curve). A narrow spectral range containing 1500-1630 nm is explicitly shown in Fig. 2.16g. Thus far, we have obtained a spectral relationship with the transmission ratio in measurements, that shows similar wavelength dependence with the simulation, but the value of the ratio is not completely in agreement with the simulation. Also, the limited spectral range of 1500-1630 nm in the measurement is due to the operating range of the tunable IR laser.

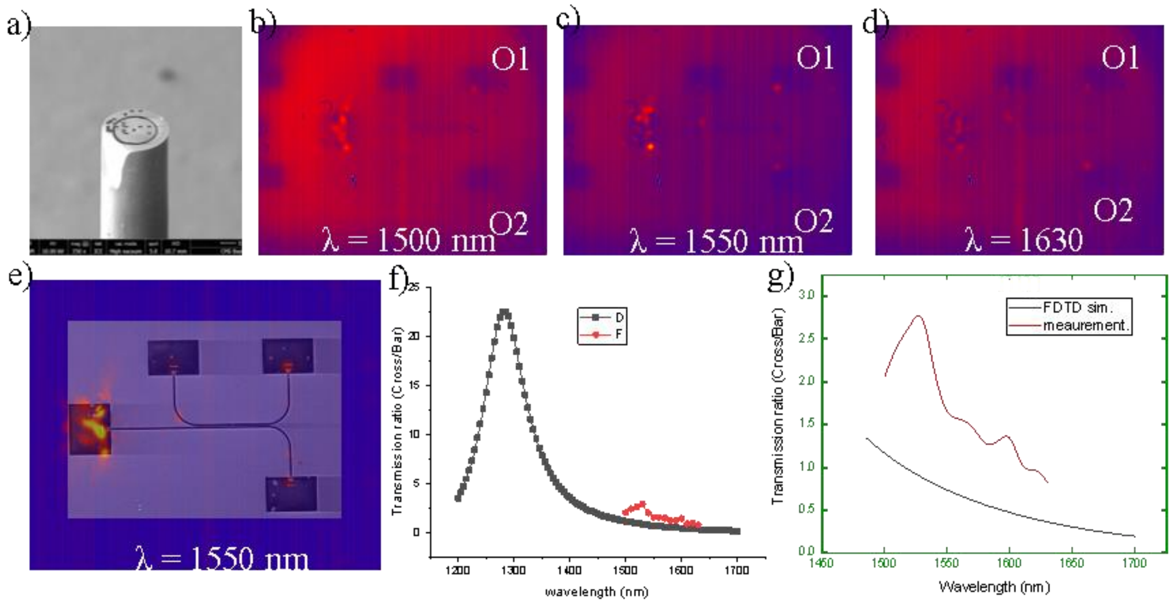

Fig. 2.16. (a) Scanning electron micrograph (SEM) image of ODC fabricated on PS fiber. Far-field measurement at wavelength of (b) 1500 nm, (c) 1550 nm, (d) 1630 nm). Far-field optical image at wavelength of 1550 nm overlayed with SEM image. (f, g) Simulated (black curve) and measured (red curve) transmission ratio between port 1 and port 2 with different spectral ranges.

To investigate larger spectral range, a CW supercontinuum (SC) laser in conjunction with bandpass filters are utilized in the far-field measurement of the ODC structure. Figure 2.17a shows the SEM images of the fabricated ODC in the facet of PS optical fiber. Figure 2.17b depicts the overlapped far-field optical measurement image with the SEM image, clearly showing the coupling of the output. Figure 2.17c shows the distinct coupling at the output antenna with the supercontinuum source when no filter was used. Figure 2.17d shows the far-field measurement when a bandpass filter at wavelength of 1480 nm with a bandwidth of ±10 nm. The measurement clearly shows the higher intensity in O1 (output 1 = cross output, intensity I_{cross}) than the O2 (output 2 = bar output, intensity I_{bar}). The almost equal intensity of both outputs O1 and O2 (Fig. 2.17e) and the higher intensities of output 2 (Fig. 2.17f) shows the power coupling in between the of 1480 nm and 1650 nm. To further show the complete switching (e.g., ON/OFF at O1/O2), a better-quality fabrication of ODC in PM-PS fiber and larger spectral measurement range is needed. Figure 2.18 shows the latest fabrication of good quality structures with thickness of gold filament separating two horizontal slot waveguides in the range of ~70nm. The optical measurement from this sample is yet to be performed.

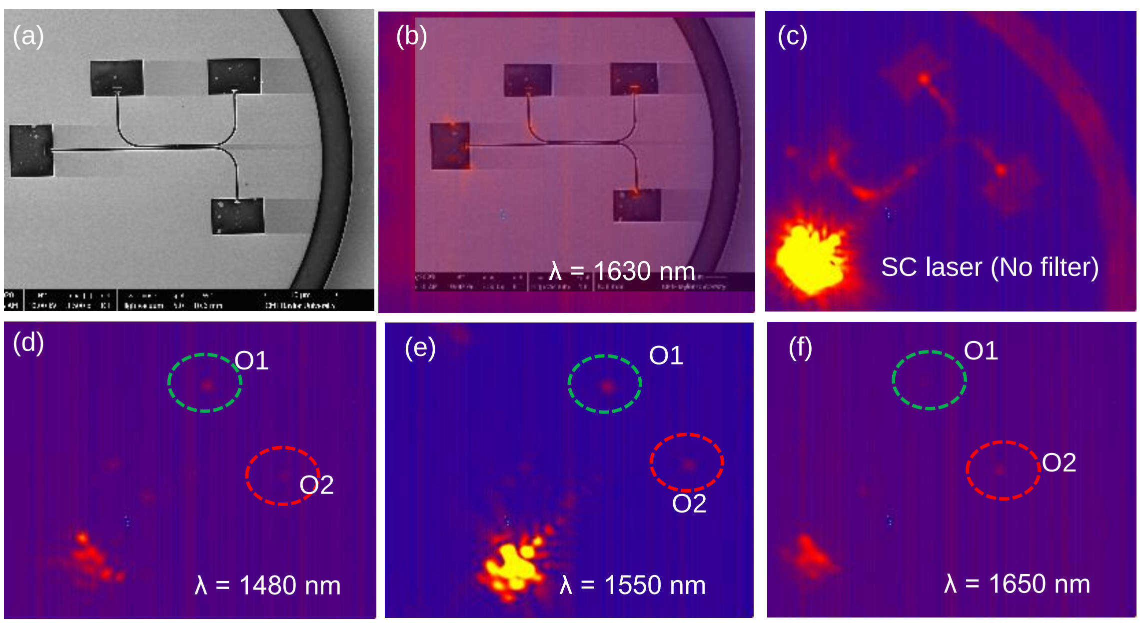

Fig. 2.17. (a) Scanning electron micrograph (SEM) image of ODC fabricated on PS fiber. (b) Overlap image of far-field measurement at wavelength of 1630 nm. (c) Far-field image of structure using supercontinuum (SC) source laser without optical filter. (d) Measured far-field optical image at wavelength of (d) 1480 nm, (e) 1550 nm, and (f) 1650 nm detected at cross-polarization to the incident radiation.

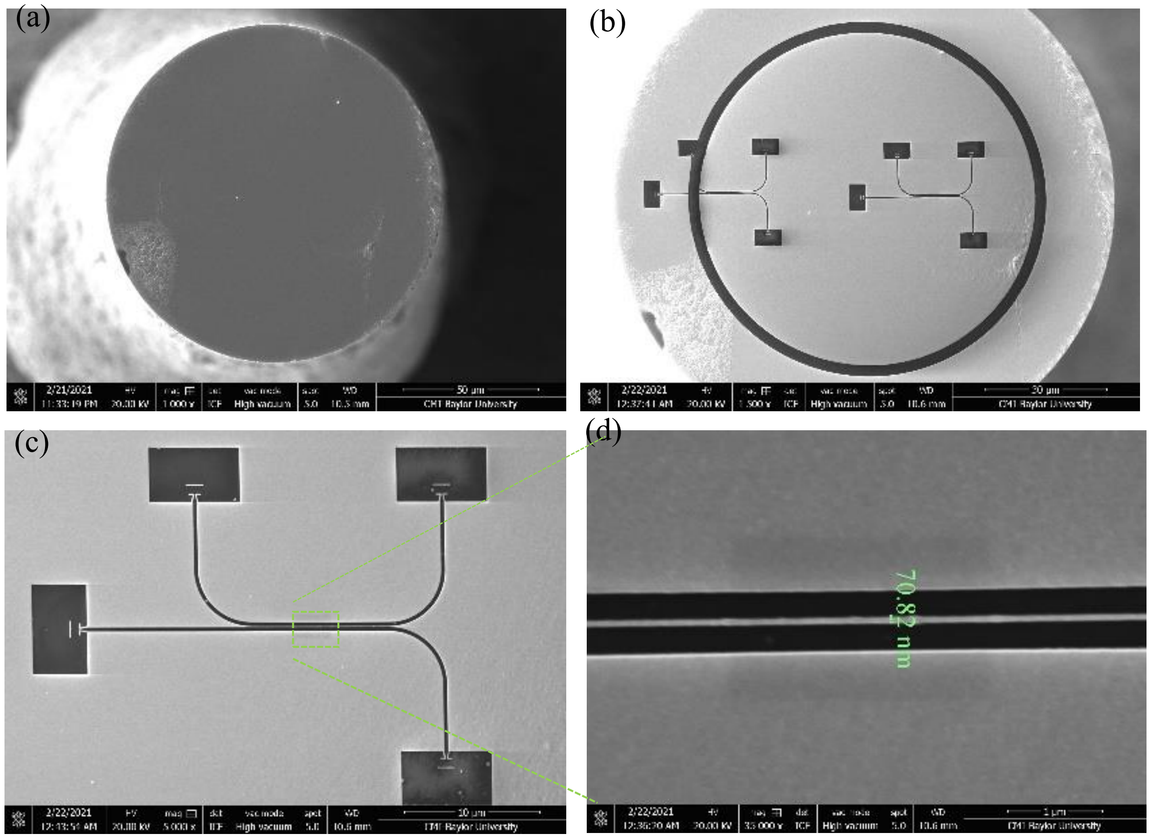

Fig. 2.18 SEM micrographs of an ODC in PS fiber facet: (a) Cleaved and gold deposited fiber (b) ODC fabricated fiber face (c) ODC in PS fiber (d) Zoom-in image of ODC showing the coupling filament of ~70 nm.

2.9 Conclusions

We have demonstrated plasmonic nano-circuits with complex structures such as multi-channel waveguides, polarization splitter, and directional coupler, on the end face of optical fiber. A simple plasmonic slot waveguide assisted with a highly efficient Yagi-Uda antenna has been investigated to reveal the coupling efficiency of the signal from the core of the optical fiber. The out-coupling efficiency from such a single waveguide at the output antenna is obtained to be ~ 0.2% after the light passes 4 µm horizontal slot waveguide section, bending portion with a radius of curvature of 4 µm and another 6 µm vertical slot waveguide section. We then utilized the multiplicative structures on the same waveguide that had four of them all originating from the core area of the fiber. Each of those waveguides is identical but with different waveguide lengths. From the multi-channel waveguides, the measured propagating loss of the plasmonic slot waveguides is 0.30 dB/μm at 1550 nm, which is close to the simulated loss of 0.28 dB/μm.

In the second section, we expanded the concept by exploiting the single waveguide as a four-straight waveguide in all four directions that are radially originating with the straight plasmonic slot waveguide assisted by Yagi-Uda antenna at each output. The structure of this design is called polarization splitters (PS-design). However, the geometry of the photonic crystal fiber (PM-PCF) restricts the design as the airy holes came across the path of the straight waveguide. This demanded us to use a different kind of fiber that does not have airy holes. We then investigated the multi-channel waveguides in polarization-maintaining Panda Shaped (PM-PS) fiber. The results from the plasmonic PM-PS fiber suggest that the emission of the desired output could be controlled by the polarization of the incident radiation. Finally, the plasmonic directional coupler structure is fabricated and demonstrated with good agreement with simulation in the narrow spectral range. Also, the switching is realized in the case of far-field measurements in the wavelength range of 1480 nm - 1650 nm.

Our work of integrating nano-circuits to the facet of optical fibers will find applications in making compact in-fiber optical devices. We believe such replacement of the chips and chips-fiber arrangement to the tip of optical fiber will revolutionize the modern compact optical devices and their portability. This work can be expanded in studying stub- resonators at THz frequencies (45) on the fiber tips and will find applications in replacing a resonant guided wave network (46, 47), and optical fiber sensing.

CHAPTER THREE

3.1 Polarization-dependent Photonic Crystal Fiber Color Filters Enabled by Asymmetric Metasurfaces.

[This work is submitted as I. Ghimire, J. Yang, S. Gurung[2], S. K. Mishra, H. W. Lee, "Polarization-dependent photonic crystal fiber color filters enabled by asymmetric metasurfaces, to *ACS Photonics* (2021)]

Optical fibers have proven to be an efficient and platform for light guiding with low optical loss, leading to a wide range of emerging optical applications such as long-distance optical communication (48), fiber lasers (49), in-fiber imaging, sensing, and laser surgery (50-55). While the dielectric optical fiber waveguide is very efficient in transmitting light, its functionality is somewhat limited by the dielectric material of the core and cladding and their optical properties such as spectral response are fixed after the fiber drawing fabrication and most of the available optical fiber components are bulky in size, thus limiting the development of novel compact in-fiber optical devices. Therefore, there is a need to integrate new materials and nanostructures into fiber components for enhanced processing and transmission capabilities, novel functionalities, and compactivity.

Metasurfaces, arrays of subwavelength elements in which each element is configured to control the phase and amplitude of the transmitted, reflected, and scattered light (5-7), provide unique ways for advanced light manipulation and development of novel applications. Because metasurfaces are by nature flat (typical thickness < 100nm), conventional three-dimensional optical elements such as lenses or filters could be replaced by flat and low-profile metasurface versions. Integrating these metasurface nanostructures on the fiber facet could facilitate their interactions with the guided core modes of the optical fibers and develop novel in-fiber optical applications.

Several initial attempts have been made to fabricate meta-structures on optical fiber for various advanced in-fiber applications, for instance, plasmonic sensors (56-60), focusing metalens (61), diffraction grating (62), amplifier(63), beam diffraction element (64), Bessel beam generation (65), and efficient fiber coupler (66, 67). These meta-structures on optical fibers are fabricated by translating the advanced on-chip nanofabrication techniques to optical fiber platform such as electron-beam lithography (60), focused ion beam milling (61), interference lithography (68), self-assembly (69), and nano-imprinting/nano transfer technologies (70-72). In particular, developing compact wavelength- and polarization-dependent optical fiber metasurface/plasmonic filter and resonant element is particularly important for optical fiber imaging, laser, and sensing applications. Few attempts have been made in this direction, including fabricating metallic structure to the polymeric membrane on the facet of a hollow-core PCF for a nano-plasmonic filter (73). However, ultracompact polarization-dependent metasurface optical filters on optical fiber have not been experimentally reported.

In this work, we experimentally demonstrate ultracompact in-fiber polarization-dependent color filters on the end face of polarization-maintaining photonic crystal fibers (PM-PCFs) and conventional polarization-maintaining optical fibers by fabricating asymmetric cross-typed nanoslit metasurface array with a thickness of 118 nm onto the optical fibers’ cores. Strongly polarization-dependent transmissions are observed at resonances of metasurface which are designed by the nanostructure’s geometry. The results suggest that asymmetric metasurface-optical fiber will have applications as in-fiber wavelength-dependent filters and polarizers for optical fiber imaging and sensing applications.

3.1.1 Design and Fabrication

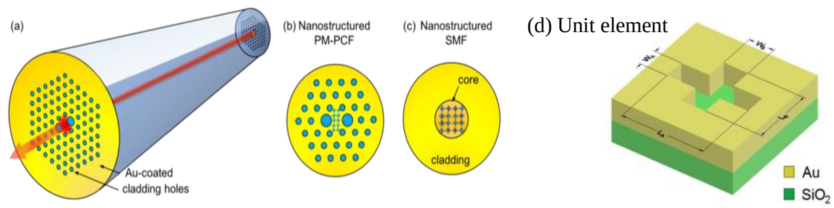

Fig. 3.1.1 Schematics of the structured fiber (a) Cross-section (b) PM-PCF with nanostructures covering the core region. (c) SMF with nanostructures on the core region. (d) Design of the unit element that is repeated over x- and y- direction to form the periodic nanostructures.

The metasurface-optical fiber color filter consists of periodic negative cross-typed metallic nanostructures with orthogonal slits (Fig. 3.1.1). A thin layer of gold with a thickness of 118 nm is deposited on the end face of the optical fiber using a magnetron sputtering technique. These periodic cross-typed metallic slits are then fabricated using a focused ion beam (FIB) milling technique with an accelerated voltage of 30 kV and an ion current of 1.5 pA. To avoid the charging effect from the silica glass, silver paste and conducting tape are used to connect between the gold and metallic fiber holder. Two types of optical fibers, conventional single-mode fiber, and PM-PCFs are used for fabrication and comparison on the optical response. The PM-PCF used in the experiments consists of a two-dimensional array of hollow channels running along the entire length of a glass strand with two large circular holes located near the core, thus providing strong birefringence for maintaining the polarization state of the light to interact with the metasurfaces. To fabricate the asymmetric structures on PM-PCF, special care is taken such that the orthogonal nano-slits are aligned with the slow and fast axes of the fiber during the FIB fabrication. The holey structures in the PM-PCF help the alignment during the FIB milling. Test patterns are first fabricated in the cladding region to ensure optimal focusing of the ion beam before positioning to the core for the actual pattern. Both symmetric and asymmetric metallic nano-slits are fabricated for studying the polarization-dependent transmission properties.

Light couple to these metallic nano-slits excites plasmonic resonance modes and re-emit through the transmission, leading to wavelength-dependent transmission peak. The transmission properties can be designed by adjusting the geometric parameters of nano-slit structures such as slit dimension, array period, and the thickness of the gold film. To find the dependence of the transmission peak on the geometric parameters, we numerically studied the optical response of the color filter using the finite element method (Lumerical) and performed parametric sweeps on the width and length of the nano cross. The gold layer thickness is fixed at 118 nm. Structure with a unit nano-cross is optimized with a wide of 180 nm and the length of horizontal and vertical arms to be 580 nm and 480 nm long respectively such that the transmission peak exhibits high efficiency (~ 80%) and is located in the telecommunication band.

The scanning electron microscope (SEM) images of the fabricated structures are depicted in Figure 3.1.2. Symmetric nano-cross array (unit element wide of 176 nm, length of slit of 490nm) and asymmetric nano-cross (unit element wide of 182 nm, length of slit of 510 nm and 419 nm) are fabricated on the core of PM-PCF with approximately rectangular core dimension of ~ 6 X 8 μm^2 (Fig. 3.1.2a). Asymmetric nano-cross (unit element wide of 193 nm, length of slit of 577 nm and 465 nm) are also fabricated on the core of conventional single-mode fiber with a core diameter of 8 μm (Fig. 3.1.2b).

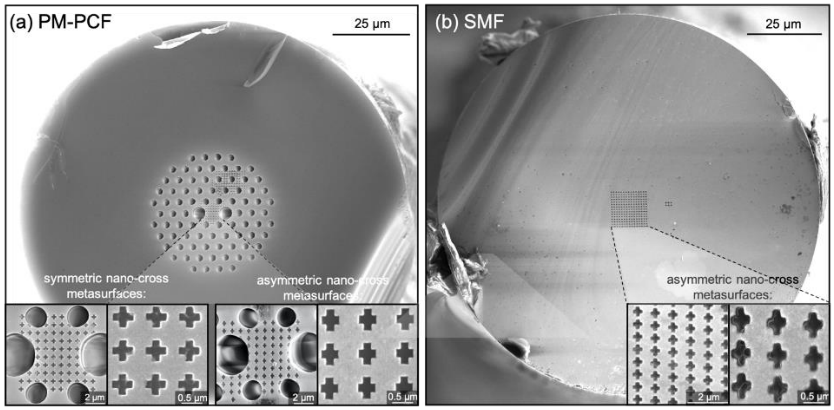

Fig. 3.1.2: Scanning electron microscope images of (a) PM-PCF. (b) PM-PCF cross-section with the symmetric cross as nanostructures covering the core region. (c) detailed cross-section of (b). (d) SMF with nanostructures on the core region (e) asymmetric cross as nanostructures on SMF. (f) detailed cross-section of (e). (g) PM-PCF with nanostructures covering the core region. (h) PM-PCF with the asymmetric cross on the core region. (i) detailed cross-section of (h).

3.1.2 Results and Conclusion

A schematic of the setup used for optical measurements is shown in Fig. 3.1.3a. Light from a supercontinuum laser source (Fianium, 4W) was launched into the fiber sample (total length ~ 13 cm), taking care to match the numerical aperture and spot size to that of the fundamental core mode. A linear polarizer and half-wave plate were inserted between the light source and the sample, providing a defined input polarization state. Light transmitted in the output end with metasurface was collected by coupling into multimode fiber core diameter of 300 μm) to the optical spectrum analyzer. The measured spectrum was normalized to that of an unpatterned fiber under the same launching conditions, thus revealing the effect of the metasurface.

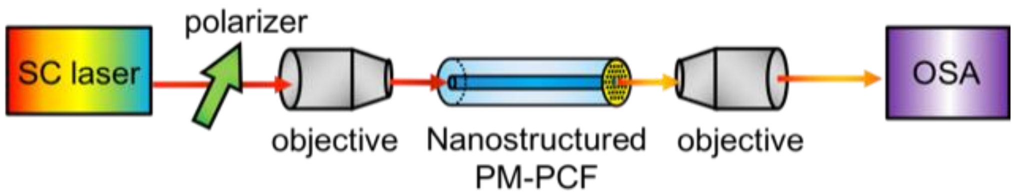

Fig.3.1.3 Schematic of optical transmission setup

To examine the effect of the metasurface, we measure the transmission spectra for x- and y-polarizations for the PM-PCF with symmetric nano-cross metasurface, and the results are shown in Fig. 3.1.3a. The length of each perpendicular slits is 490 nm and the width of 176nm. Two orthogonally polarized light along the slow/fast axis of the PM-PCF is launched into the fiber. Clear transmission resonant peak is observed at the wavelength of ~ 1460 nm for both horizontal and vertical polarization states with a transmission efficiency of ~70%. A full-wave electromagnetic simulation was performed with the same fabricated metasurface geometry and the results are shown in Fig. 3.2.3b. Good agreement is obtained comparing the simulations and the measurements on both the resonant wavelength and the transmission efficiency.

Next, we explore the polarization dependence of the PM-PCF with asymmetric nano-cross metasurface with slit lengths of 510 nm and 419 nm (Fig. 3.2.2a, right). The metasurface structures are precisely aligned so that the long arm of the nano-cross is along the slow axis of the PM-PCF. Since the polarization state of light can be preserved in the PM-PCF, horizontal or vertical polarization states of the light are ensured to interact with the desired axis of the nano-cross metasurface. As shown in the measurement results in Fig. 3.1.4a, distinct transmission resonance peaks located at the wavelength of 1350 nm and 1620 nm are observed for the horizontal and vertical polarization states, respectively.

Numerical simulations were performed, and the spectral positions of the simulated transmission peaks (1350 nm and 1630 nm) closely match those of the experiments. In x-polarization, the fundamental core mode of the optical fiber is coupled strongly with the plasmonic resonance with the short arm of the nano-cross, leading to a shorter resonant wavelength and lower transmission efficiency compared to the resonant peak in the y-polarization state. The slight discrepancy between measurement and simulation might attribute to the non-uniformity and non-ideal shape of the fabricated nanostructures.

Finally, we investigate the color filtering properties in the conventional single-mode fiber integrated with an asymmetric nano-cross metasurface array. In this measurement, unpolarized light was launched into the fiber and a polarizer was used in the output of the fiber to selectively collect the x- or y-polarization of the transmitted light. As shown in the measured spectra in Fig. 3.1.4a, similar to the case in meta-structured PM-PCF, transmission peaks are observed at the wavelength of 1400 nm for x-polarization state and at 1650 nm for the y-polarization state. The resonance peaks are located in a longer wavelength than in the case of meta-structured PM-PCF because of the slightly larger fabricated structures (Fig. 3.1.2 b). These results indicate that the metasurface color filter can be routinely realized in any conventional optical fiber and can be used as a wavelength-selective filter and polarizer.

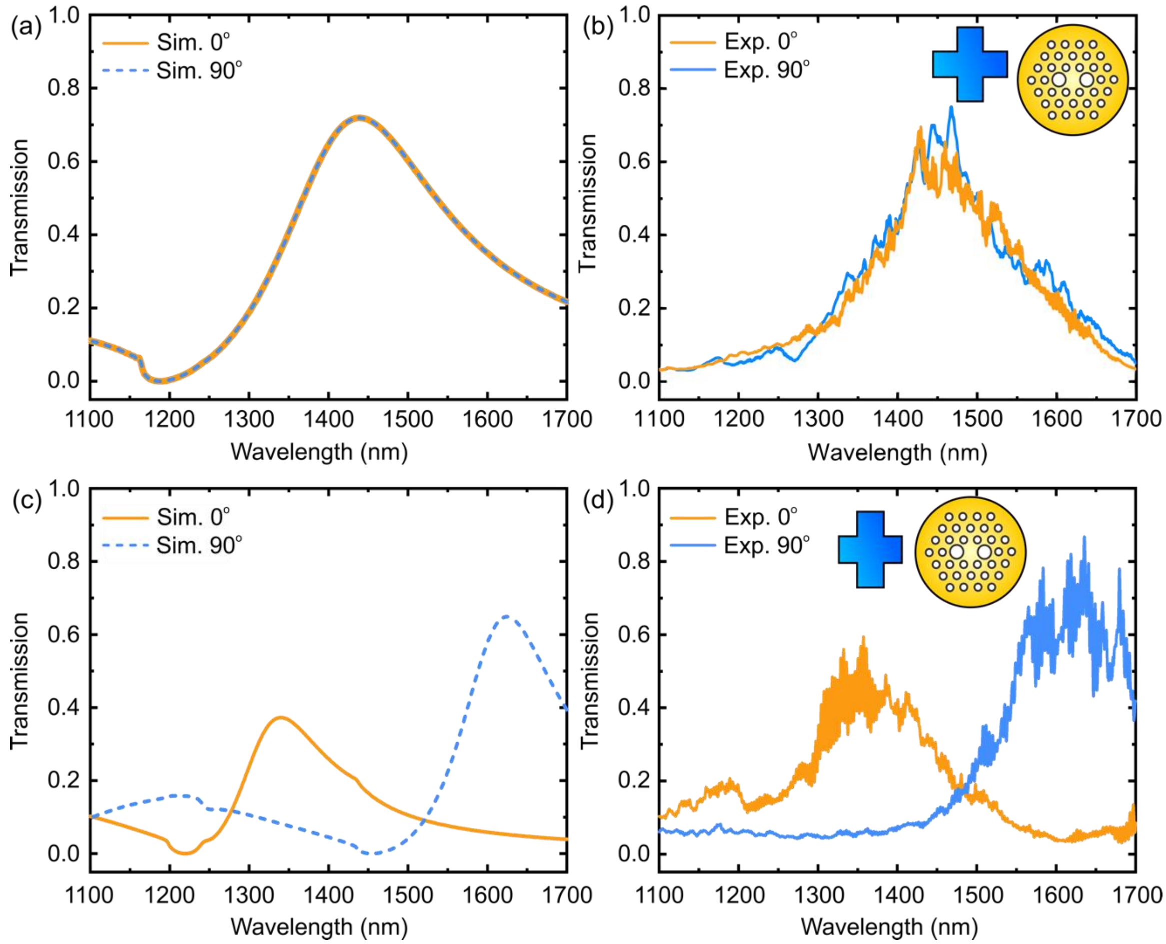

Fig. 3.1.4. Transmission Spectra for PM-PCF metasurface color filter. (a) Simulated and (b) measured transmission spectra for x- and y-polarization states for PM-PCF with symmetric nano-cross metasurfaces. Symmetric nano-cross array has unit element wide of 176 nm and length of the slit of 490 nm. (c) Simulated and (d) measured transmission spectra for x- and y-polarization states for PM-PCF with asymmetric nano-cross metasurfaces. Asymmetric nano-cross consists of a unit element with wide of 182 nm and a length of slit of 510 nm and 419 nm.

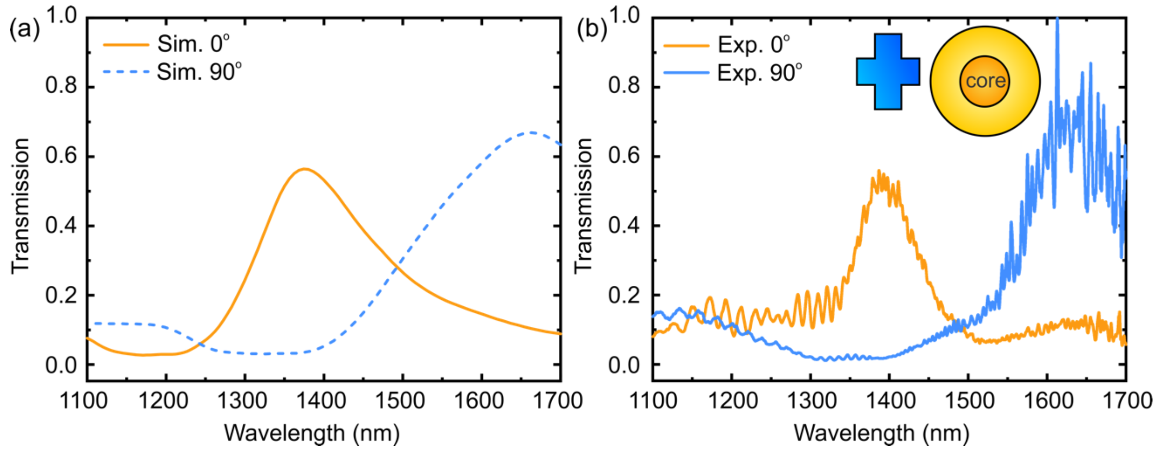

Fig.3.1.5. Transmission Spectra for metasurface color filter in SMF. (a) Simulated and (b) measured transmission spectra for x- and y-polarization states for SMF with asymmetric nano-cross metasurfaces. Asymmetric nano-cross consists of a unit element with wide of 193 nm and length of slit of 577 nm and 465 nm.

We experimentally demonstrate a polarization-dependent in-fiber color filter with an ultrathin asymmetric metasurface patterned on the fiber end face by focused ion beam milling technique. Highly polarization- and wavelength-dependent transmission with transmission efficiency ~ 70 % in the telecommunication wavelength are observed by launching light into two orthogonal linear polarization states of the fiber. The operation wavelength of the metasurface color filter could be widely controlled by nano-engineering the metasurface's geometry. This work provides a new paradigm for developing nanoscale in-fiber devices such as in-fiber polarization- and wavelength-dependent filters, polarizers, metalens for emerging optical fiber imaging and sensing applications.

Numerical simulation of the nanostructures on the fiber is carried out using full-wave simulation of Finite Domain Time Difference (FDTD) software from Lumerical Solutions, Inc. For the simulation, a unit cell is designed, and a full-wave simulation is carried out with periodic boundary conditions along x- and y- boundary with a finer mesh size which is tallied with a full simulation with the whole periodic structure. The polarization-maintaining photonic crystal fiber PM-PCF used is pure silica glass (Thorlabs, PM-1550-01). The PM-PCF consists of two special holes, which distinguish from all other holes and reduce the six-fold symmetry to a two-fold one. The presence of two large holes adjacent to the core introduces birefringence in the fiber, leading to a phase index difference between the x- and y- states. The diameters of the large and small holes are 4.4 µm and 2.5 µm, respectively.

3.1.3 Metalens in Single-mode Fiber (SMF)

This chapter published as a part of as: J.Yang, I. Ghimire, P. C. Wu, S. Gurung, C. Arndt, A. D. P. Tsai, H. W. Lee, "Photonic crystal fiber metalens", *Nanophotonics* 8, 443-449 (2019).
And,
HWH Lee, J. Yang, I. Ghimire, US Patent 10,838,129 (2020)

Optical fibers, due to their very effective light-guiding mechanism have proven successful in signal transmission medium over a long distance for decades. The importance of optical fibers cannot be exaggerated as their application ranges from fibers lasers (74, 75), medical endoscopy (76), fiber imaging (77), laser surgery(78, 79), sensing (80), and generation of random laser (81). Out of many optical properties of fiber, that are fixed once after the fabrication from the fiber drawing tower, the focus is one of the most important and cannot be overlooked. The light coming out from such optical fibers is not collinear, focused but rather divergent. This divergent nature of the emitted light will be troublesome in most cases especially when we need a highly focused light.

Most of the conventional optical components we use today are bulky, costly, and difficult to make with high precision (82). For example, many people wear glasses with a thickness in the range of several millimeters. In a typical optics laboratory, the objective lenses we use today are big enough that they cover a significant amount of space in the setup. Such bulky optical components are to be replaced by miniaturized ones. With the advent of new fabrication technologies, compact optical devices can be designed and realized due to tiny elements with a size in subwavelength scale, called metasurfaces, which are able to shape the wavefront and thus precisely control the phase. Some of these compact optical devices include the meta structures in flat lenses (83),(84), polarization elements (85, 86), holograms (87-89), broadband achromatic metalens (90), etc. Numerous studies on incorporating these metasurface elements on the optical fiber platform to invent miniaturized in-fiber devices and also modify the optical properties of such fiber have been going on. Some of these recent studies include diffraction grating (91, 92), optical tweezer (93), nano-trimmers (94), plasmonic sensors(95, 96), and endoscopic imaging applications (97). Here, we aim to realize the metalens by incorporating these metasurfaces directly on the facet of optical fibers to design and demonstrate in-fiber metalens. Such kinds of fiber metalens may find applications in optical sensing and medical imaging.

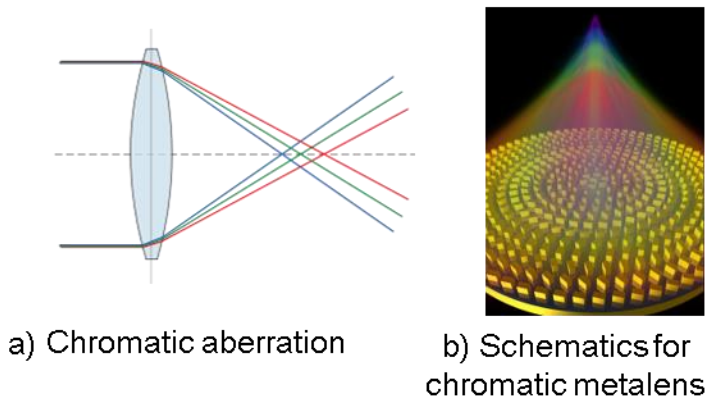

Fig. 3.2.1. Metalens: a) Chromatic aberration: different wavelength (color) has focus on different distances b) a schematic of a metalens.

Figure 3.2.1 depicts the metalens, which is composed of tiny elements aligned in such a way that the phase profile from them gives rise to a focusing effect. The chromatic aberration is shown in fig.1a which illustrates that different wavelengths have different focal lengths. Fig. 3.2.1b shows the arrangement of tiny elements giving a focusing effect with each color focused on a different distance from the surface.

3.2.1 Design and Working of the Berry-phase Metalens

A Berry-phase metalens consists of an arrangement of tiny slits on a metallic surface that gives the gradual phase change. Such phase retardation is given by the equation,

$$\varphi(r, \lambda) = -\frac{2\pi}{\lambda}(\sqrt{\gamma^2 + f^2} - f) \quad \text{..................................(3.2.1)}$$

Where r is the radial distance from the center of the metalens and f is the desired frequency and the $\boldsymbol{\lambda}$ being the operating wavelength.

Metallic slits/nano-antenna of exactly similar dimensions are arranged as the metasurface elements where a uniform gold-sputtered surface has been employed for fabrications and the negative metasurface (slits) are patterned. The rotational angle (angle between the slit length and the y-axis) of each antenna (rectangular slit) is varied as it goes radially outward. A unique pattern of the periodicity of such elements is generated using a pattern generator, namely, AutoCAD, and the design is imprinted over the targeted surface.

3.2.2 Sample Fabrication and Transmission Setup

Single-mode optical fiber is first cleaved, and a layer of gold is sputtered on the top of the fibers using an RF magnetron sputtering machine. The thickness of the gold layer is ~ 40 nm, which is determined by the time of active sputtering, the vacuum pressure of the sputtering chamber, and temperature. Thus, gold deposited fibers are deployed in a Scanning electron microscope (SEM) where a focused ion beam (FIB) is utilized to fabricate the metasurface structures. The design file is priorly generated according to the simulation estimates using the pattern generator and the gallium ion (Ga+) performs the patterning on the surface, a process called FIB milling. Among the available parameters, we have used 1.5 pA ion current and 30 kV accelerating voltage for the ion beam for our sample fabrications. The choice of these current and voltage is a way to get the best quality of the metasurface. A higher ion beam current would reduce the time of the fabrication but degrades the quality.

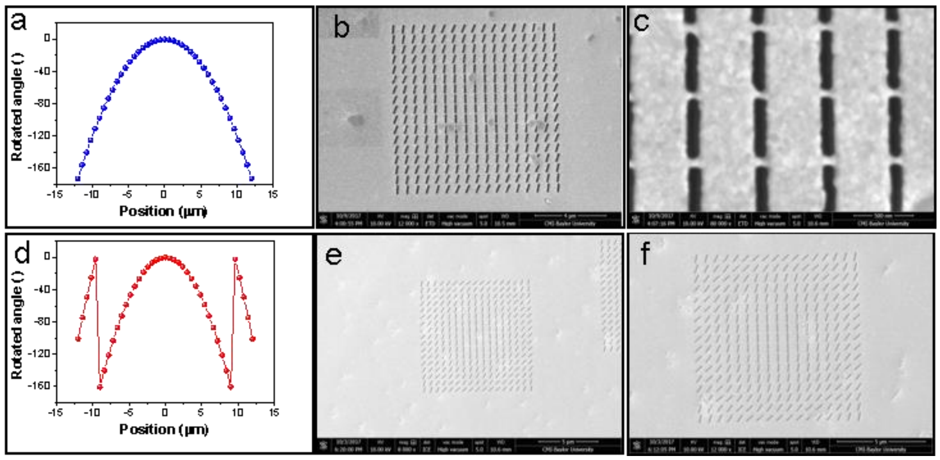

Fig.3.2.2. Metalenses (a) Design for metalens 1 (M1) (b) SEM micrographs of fabricated metalens (M1) on an SMF fiber (c) Zoom-in image of M1 (d) Design for metalens 2 (M2) (e) SEM micrographs of fabricated metalens (M2) on SMF (f) Zoom-in image of M2.

Figure 3.3.2 illustrates the designs and first fabrications of metalenses on the fibers. This consists of two metalens designs. The first metalens design, namely M1 (fig. 3.2.2a) has a focal length of 50 µm, a diameter of 24 µm, and a numerical aperture (NA) of 0.2334. The SEM image of the fabricated metalens on a single-mode fiber is shown in fig. 2b and its zoom-in image in 3.2.2c. Fig. 3.2.2d shows the design of the second metalens (M2) which has a focal length of 30 µm, a diameter of 24 µm, and a numerical aperture of 0.3714. Figure 2e shows the SEM micrographs of the fabricated metalens M2 on SMF with fig. 2f as the zoom in the image.

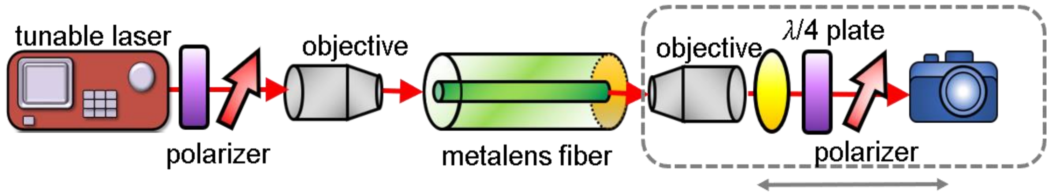

Fig.3.2.3 Far-field measurements setup.

The fabricated fiber metalenses were then brought to the optical transmission setup where the far-field optical measurement was performed. A tunable laser source was used for inputting a signal that couples through free space to a linear polarizer and then to a quarter waveplate ($\boldsymbol{\lambda}/4$) in such a way as to generate a circularly polarized light. This laser was then focused on the optical fiber using an objective lens and coupling is done in such a way that we get maximum possible light transmitted through the fiber which is a core mode of the fiber. Such a transmitted light then interacts with the metasurface elements on the end facet of the structured fiber which is expected to show the focusing effect. The optical components, including the objective lens, quarter waveplate, linear polarizer, and an IR camera at the output end, are attached to a translational piezo stage. The IR camera is used to record images from the optical fiber when the piezo is moved at every unit of its smallest possible translation along with the + ve z-axis (away from the fiber). We are invested in two circularly polarized lights which are right-hand circular polarization (RCP) and left-hand circular polarization (LCP). An RCP light is launched from the input end and both RCP and LCP are detected at the output. The angle between the linear polarizer and the quarter waveplate determines the handedness of the polarized light. Two different sets of camera images, one for each handedness (RCP or LCP) at the output are recorded and are further analyzed for their intensity distributions.

3.2.3 Characterization and Simulation

The metalens design is characterized and simulations are performed to understand its mechanism prior to the fabrication. A unit cell consists of a metallic slit of 450 nm length, 75 nm width, and a periodicity of 500 nm along each direction (x-axis and y-axis) as shown in figure 4b. Finite Difference Time Domain (FDTD) Lumerical simulations are performed to determine a rotational angle for each element that gives a profile for rotational angle vs. radial distance from the center of the metalens as shown in Fig. 4d. For example, the nano-antenna / slit right at the center of the core of the fiber has zero rotation, i.e., it is aligned along the y-axis. As the metalens goes radially outward the rotation angle increases, which ultimately gives rise to the phase profile resulting in a demonstration of the focusing effect, as suggested by equation 1 and shown in Fig. 4c. Fig. 4e shows the conversion efficiency (RCP to LCP) as a function of wavelength for the optimized unit element.

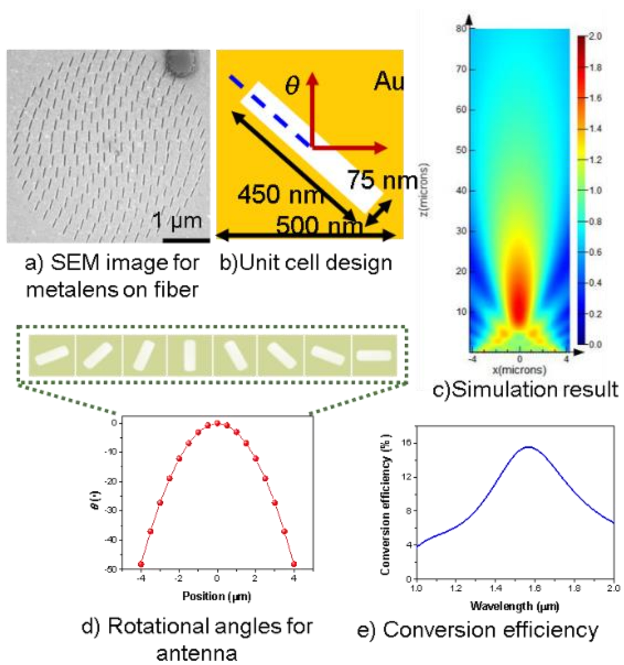

Fig.3.2.4. Characterization of metalens: (a) SEM micrographs of a metalens fabricated on SMF (b) A basic unit element (c) Simulation result showing the focusing effect (d) Angular rotation design for the type of metalens (e) Simulated conversion efficiencies.

3.2.4 Result and Discussion

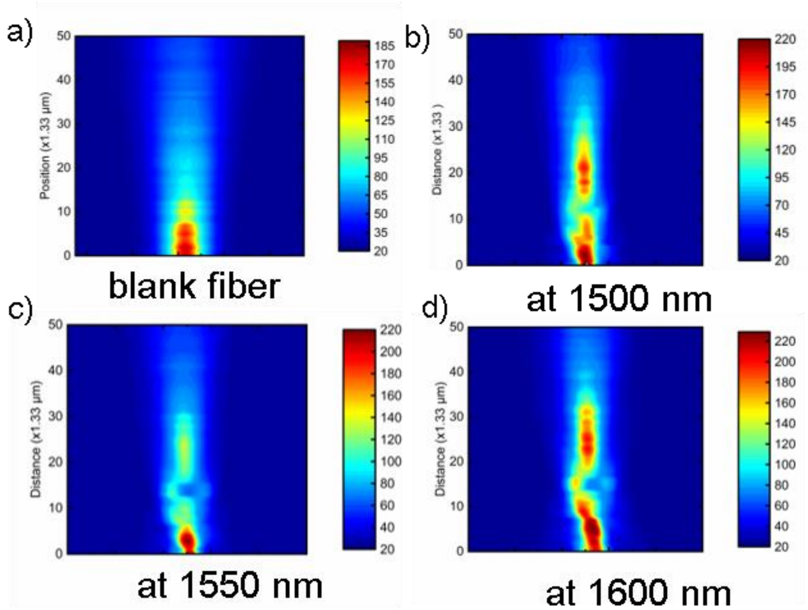

Fig.3.2.5. Far-field measurements: (a) Blank fiber for reference; From the structured fiber at a wavelength of (b) 1500 nm (c) 1550 nm (d) 1600 nm.

As discussed earlier, the fabricated in-fiber metalenses are used for the far-field measurement in the setup as shown in figure 3.2.3. Two different sets of measurements (RCP to LCP and RCP to RCP) are performed and a series of images from the IR camera are recorded. The RCP light is exercised as the phase modulation is only realized on these circularly polarized lights and the output is detected at both the RCP and LCP configuration. Similar measurements are performed for the bare fiber (with no gold layer and no meta structures) for normalization as a reference SMF. The results show that the conversion efficiency as high as 16% is achieved for the RCP-LCP configuration.

Figure 3.2.4 shows the experimental measurements from the blank and metalens SMFs.The measurement shows that our piezo stage can be moved one unit (pitch) and each unit movement is 1.33 µm. In this way, the distance moved along the +ve z-axis is determined that is analyzed with each image recorded on camera, and their corresponding intensities are analyzed. These measurements are repeated at three different operational wavelengths: 1500 nm, 1550 nm, and 1600 nm, all shown in figures 3.2.5b, 3.2.5c, and 3.2.5d, respectively. Figure 3.2.4 shows that for 1550 nm, the focus is obtained for ~ 32 µm which is very close to the design of 30 µm, metalens M2.

3.2.5 Conclusion

We have thus far successfully established a direct fabrication way of building in-fiber metalens in SMF. Our group has been able to demonstrate the Photonic crystal fiber metalenses in Large Mode Area Photonic Crystal Fiber (LMA-PCF) of focal lengths of 28 µm and 40 µm at 1550 nm with maximum optical efficiency as high as 234%[(61, 98)]. This present chapter deals on the metalens fabrication using metallic (gold) nano-antenna as a negative metasurface element. Our group has simulated the performance of Silicon nano-antenna that is optimized as a unit element and simulated to exhibit 91% efficiency at an operational wavelength of 1550 nm. This work of designing such ultrathin in-fiber metalenses can be further explored in electrical tunability. Such in-fiber metalens might find their potential applications in performing highly focused fiber lasers and are suitable for nano-imaging.

CHAPTER FOUR

4.1 Active Excitation of Plasmonic Resonance in Vanadium Dioxide Coated Anti-Resonant Nodeless Hollow-Core Fiber

This work published as Q. Huang, I. Ghimire, J. Yang, N. Fleer, K. S. Chiang, Y. Wang, S. Banerjee, H. W. Lee, “Optical modulation in hybrid anti-resonant hollow-core fiber infiltrated with vanadium dioxide phase change nanocrystals”, *Optics Letters* 45, 4240 (2020).

.

Vanadium dioxide (VO2) is a remarkable optical material with a material phase transition from insulating to metallic states at a transition temperature in reasonable proximity to room temperature(99-110). Since the metallic state of these materials can be actively controlled, it has been used for various unique planar plasmonic applications, for instance, controlling the polarization of light(99), modulating optical phase and amplitude of metasurfaces/ metamaterials(100-104); altering the coupling of the optical nanoantenna (106), and optical sensing (107). In addition to its use in planar structures, this functional VO2 material has also been integrated within on-chip waveguide platforms to form devices, such as hybrid plasmonic modulator (111), silicon waveguide optical modulator(112), silicon waveguide-based compact TE and TM pass polarizers(113), and optically triggered nanoscale memory devices(114). The optical switching and thermal recovery properties of VO2 have been applied to realize an optically controlled temperature-dependent fiber modulator(115). An all-fiber liquid level sensor using the VO2 doped fiber has also been reported(116).

Anti-resonance hollow-core fibers (AR-HCFs) provide many advantages over conventional optical fibers and hollow-core photonic crystal fibers, for instance, broadband single-mode operation, low-loss hollow-core transmission, and high waveguiding damage threshold, leading to novel applications in fiber lasers, biosensors, and quantum optics, etc.(117). The AR-HCF can provide relatively low loss propagation in the hollow core (~100 dB/km) and a bending loss of ~0.2 dB/m at a 5 cm bend radius at the telecommunication wavelength(118). The design, fabrication, characteristics, and advantages of the AR-HCF are summarized in Ref. (118-120). In this paper, we report the integration of tunable nanocrystalline VO_2 material into AR-HCFs to achieve active optical function. We demonstrate optical modulation in VO_2-filled AR-HCF by changing the ambient temperature to the phase transition temperature of 53 ºC. We obtain an amplitude modulation larger than 60% in an ultra-broadband spectral range (which encompasses the S+C+L band) with a 3-cm long AR-HCF filled with VO_2.

4.2 Fabrication and Measurement

The AR-HCF that we used was fabricated by the stack-and-draw technique(118, 119). A schematic of the VO_2 AR-HCF and scanning electron micrographs (SEM) of a bare fiber are depicted in Fig. 4.1(a), and 4.1(b), respectively. The AR-HCF is made with silica glass and consists of a 50-µm air hole with six 10-µm rings attached inside. The large hollow core allows the filling of mixed organic nanoparticles (VO_2 nanocrystals) with standard capillary force. The measured transmission spectra of a 20-cm long blank AR-HCF are shown in Fig. 4.1(c), showing the typical broadband single-mode transmission property of the fiber. The transmission loss of this AR-HCF is about 0.02 dB/cm at 1550 nm(119). Alkylsilane functionalized ultrasmall VO_2 nanocrystals diluted by hexane were used in the experiment. An injector was utilized to fill the VO_2 liquid into the fiber. After that, the fiber was heated under a temperature of ~50 ºC to solidify the VO_2 liquid. Since the hexane evaporated quickly when the ambient temperature increased, a layer of VO_2

nanowires was deposited uniformly in the fiber. Note that most of the VO2 nanowires, deposited by the evaporated hexane gas was concentrated at both ends during the

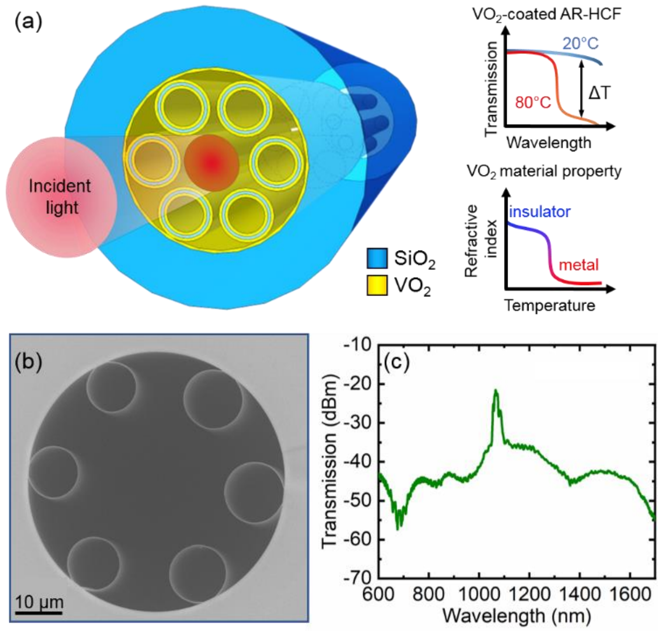

Fig. 4.1 (a) Schematic of the VO_2 Infiltrated AR-HCF. (b) SEM image of the AR-HCF. (c) Measured transmission spectrum of a 20-cm long AR-HCF, showing the broadband transmission properties of the fiber

solidification process. Therefore, both ends of the AR-HCF were cleaved about 2 cm from the ends, leaving a thin film VO2 coated on the surface of the remaining fiber. The details on the synthesis and characterization of VO2 films can be found elsewhere(121, 122). To measure the optical properties of the AR-HCF and the VO2 coated AR-HCF, supercontinuum light was launched into the sample through an objective lens with a numerical aperture matched to the fundamental core mode. The output spectrum was recorded with an optical spectrum analyzer. A polarizer was inserted between the light source and the sample to provide a defined polarization state.

To gain insight into the optical behavior of the VO2 coated AR-HCF, we carried out full-wave electromagnetic simulation by using the finite element method (FEM) (COMSOL). Pure VO2 nanowire layers are assumed to be coated in the large air hole and six rings uniformly. The refractive index (n) and the extinction coefficient (k) of the VO2 thin film at different temperatures are taken from reported values obtained from spectroscopic ellipsometry(123). The insulator to the metallic phase transition could be varied in a certain temperature range due to different fabrication conditions and the nucleation limited nature of the transition, which is correlated with the crystallite size(124).

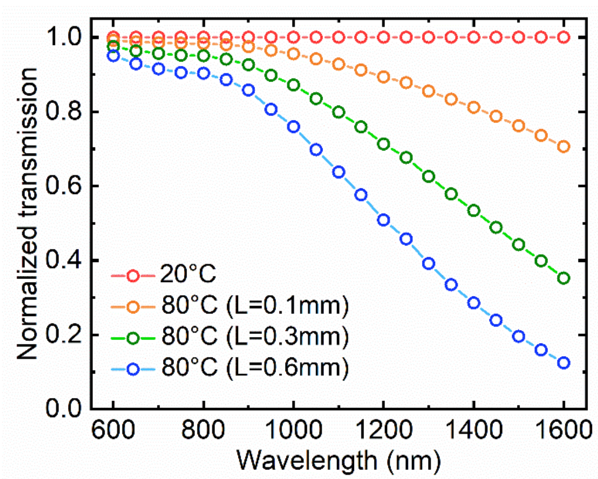

Fig. 4.2. Simulated normalized transmission spectra of the VO_2 filled AR-HCF under 20 ºC, and 80 ºC with different lengths (L = 0.1, 0.3, and 0.6 mm)

The real part Re(neff) and the imaginary part Im(neff) of the effective index of the core mode of the AR-HCF is calculated. The modal loss can be calculated as

$P_{Loss}(dB/\mu m) = 10\ log_{10}[e^{2k_0 Im(neff)}]$,……. ….. (1)

where $k_0 = 2\pi/\lambda$ is the free-space wavenumber and λ is the free-space wavelength(125). The simulated transmission spectra of the VO2 filled AR-HCF at 20 ºC, and 80 ºC for different fiber lengths, 0.1, 0.3, and 0.6 mm, are shown in Fig. 2. The spectra are normalized with that calculated at 20 ºC. As shown in Fig.4.2, the loss of the VO2-filled AR-HCF increases at 80 ºC, and the loss is dependent on the filled fiber length and the wavelength. For fiber lengths, 0.3 mm and 0.6 mm, modulations larger than 50 % and 80 % in the wavelength range that covers the telecommunication S+C+L band are achieved, respectively. The transmission dip that occurs in the longer wavelength range (from 900 nm to >1600 nm) is attributed to the VO2 changing from the insulator state to the metallic state, and hence causing the strong optical loss in the near-infrared region(122, 126).

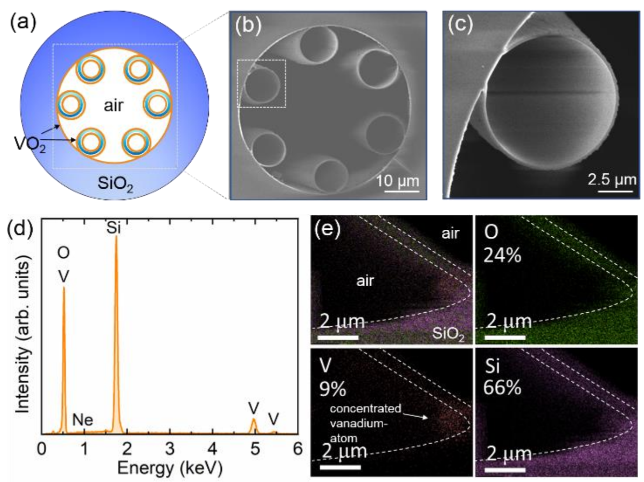

Fig. 4.3. (a) Schematic of the VO_2 filled AR-HCF. SEM images of the (b) middle section and (c) one of the holes (enlarged). (d) EDX spectra of the VO_2 material on optical fiber and (e) map of the percentage of the element atoms.

Figure 4.3(a) is a schematic of the cross-section of the VO2 AR-HCF. Fig. 3(b) and Fig. 3(c) depict the scanning electron microscope images of the VO2-coated AR-HCF after cleaving the end faces. As shown in Fig. 3, the thin films coated on the surfaces of the holes have a thickness of several nanometers. The results are similar in the middle section and at the end of the remaining fiber, as confirmed in the experiment.

Energy-dispersive X-ray (EDX) material analysis was used to identify the composition of the atoms in the VO2-filled AR-HCF. The EDX spectra are shown in Fig. 4.3(d). Every element of the VO2 filled AR-HCF has characteristic peaks of unique energy. Composition distribution maps measured using EDX are shown in Fig. 4.3(e) with the percentage of the existent atoms written in the images. The majority (about 66%) is the silicon atom and the second is the oxygen atom (24%), while the vanadium atom is only 9%. However, such a small proportion of vanadium atoms can already make a tremendous change to the optical properties of the AR-HCF. As shown in Fig. 4.3(e), the vanadium atoms are mainly located in the crossing of the rings and sidewall of the big air hole; as a result, the filled sample might be slightly different than the simulated one and a longer length of fiber could be required to observe the transmission dip compared with the modeling study.

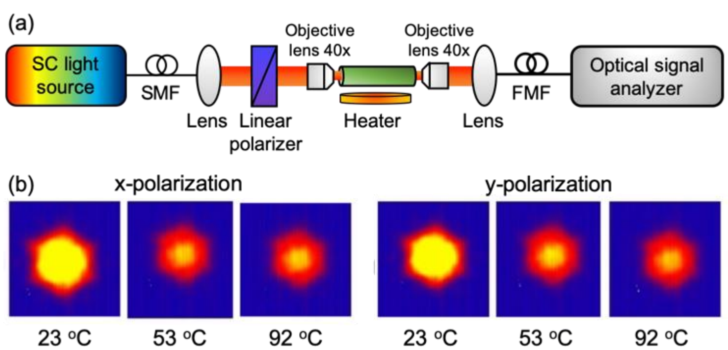

Fig. 4.4. (a) Setup for the measurement of the transmission spectrum of the VO_2-filled fiber. (b) Near-field optical images were taken at 23 ºC, 53 ºC, and 92 ºC at 1550 nm for both x and y polarizations.

The setup for the measurement of the transmission spectrum of the VO2-filled fiber is shown schematically in Fig. 4.4(a). Free-space coupling was used to launch the supercontinuum light to the VO2- filled fiber with a 40 X objective lens, and the transmitted light was collected with another objective lens and optical spectrum analyzer. The AR-HCF was placed on a heater for the control of its temperature. In this experiment, the AR-HCF used is about 11 cm long, and the heated region is about 3 cm. We also measured the light transmission at different temperatures at the wavelength of 1550 nm by using an infrared camera. As shown in Fig. 4.4(b), the light intensity (mainly the fundamental mode) decreases when the temperature increases from 23 ºC to 53 ºC. There are no further significant changes when the temperature is raised to higher than 53 ºC. The characteristics of the device are polarization independent due to the six-fold symmetric geometry of the fiber. As mentioned earlier, the temperature required for VO2 to change from the insulator state to the metallic state may vary with different fabrication conditions (123, 124). The light intensity changes measured against the heating temperature are shown in Fig. 5 (the red-triangle curve).

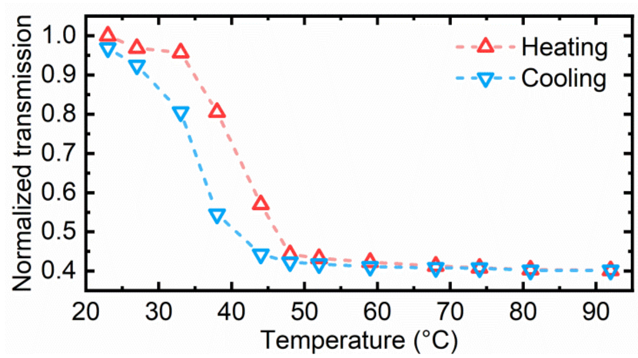

Fig. 4.5. Variation of the normalized transmission with the heater temperature at 1550 nm.

The variations of the normalized transmission of the fiber measured by heating or cooling the fiber are shown in Fig. 6. The transmission changes from 100% to 40% when the temperature changes from 23 ºC to 53 ºC, and there is no further change when the temperature increases further. In the cooling step, the transmission can almost return to the initial value when the temperature drops back to ~23 ºC. The measurements are repeated four weeks later, where the experimental results are almost the same. Our experiments confirm that the transmission characteristics of the fiber are repeatable since the VO_2 nanocrystals can normally be cycled over thousands of cycles without degradation(127, 128).

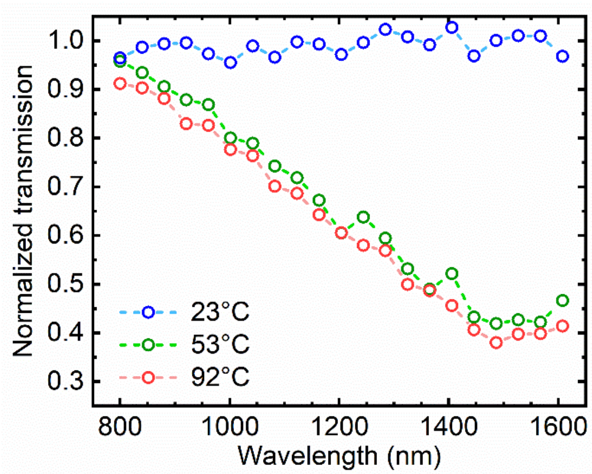

Fig. 4.6. Normalized transmission spectra of the VO_2-filled AR-HCF measured by heating the fiber from23 ºC to 53 ºC and 92 ºC and cooling down to 23 ºC.

As shown in Fig. 4.6, the loss band encompasses the S+C+L band with a loss-modulation depth larger than 60 %. Also, the loss band does not change significantly with the temperature above 53 ºC and the normalized transmission is almost restored to 100 % when the fiber is cooled down to 23 ºC. The heated length of the AR-HCF (~3 cm) is limited by the heater setup. Larger modulation could be achieved with a longer heating length. According to a previous study, the bending loss of this AR-HCF is ~0.2 dB/m at a 5 cm bend radius. It should be possible to increase the heated length of the AR-HCF by using a disk-like heater. The loss of the VO2-filled AR-HCF is calculated to be 0.45 dB/cm by comparing it with a bare unfilled fiber with the loss of ~0.02 dB/cm, which was further confirmed by using the cutback method at the room temperature of ~20 ºC. By connecting a VO2-filled AR-HCF to single-mode fibers at both ends could increase the effective heating length and reduce the length of the filled fiber. It should also be noted that the ultrafast phase transition of VO2 could be achieved by ultrafast pulse excitation(128, 129), providing another opportunity for ultrafast optical switching/modulation based on the VO2-AR-HCF. The response time could reach few tens of femtosecond with a UV-pumped femtosecond laser pulse excitation (128).

In summary, we demonstrate tunable in-fiber modulation using VO2 thin film-filled AR-HCF, which reveals a broadband light-matter interaction via the temperature-dependent phase transition of VO2. The experimental result shows that this device can achieve a polarization-independent modulation bandwidth encompassing the S+C+L band. The modulation depth can be further increased by increasing the active region length or the VO2 concentration. This in-fiber active optical device could find applications for optical fiber communication and imaging, such as serving as an efficient optical modulator, a variable optical attenuator, and a fiber sensor. In addition, the active VO2 in-fiber device could be further developed into an ultrafast all-optical controlled switch, where an ultrafast laser pulse is used to induce the insulator-to-metal phase transition.

CHAPTER FIVE

Conclusion

The works during my graduate study incorporated several projects that led to the successful demonstration of in-fiber optical devices. The integrations of plasmonic nano-circuits and metasurfaces on optical fibers are one of the main focuses of my dissertation. Also, the incorporation of vanadium dioxide nanocrystal into the airy holes of antiresonant hollow-core photonic crystal fiber (ARHCF) supplements the study of light matter in novel active platforms of optical fibers.

The initial works of integrating nano-circuits involved designing and fabricating nanostructures on the end face of the optical fibers. The dual-beam focused ion beam scanning electron microscopy (FIB-SEM) has been implemented to fabricate plasmonic nanostructured fiber samples. The first part involves the integration of a single plasmonic slot waveguide onto the optical fiber's end face. We demonstrated that a significant amount of coupling efficiency of 0.2 % was achieved by coupling directly from the core of the optical fiber. This coupling efficiency was measured by taking into account the in/out-coupling of the Yagi-Uda antenna, the long plasmonic slot waveguide region, and the bending losses of waveguides. The design is then further modified to investigate the multiple channel waveguide that is fabricated on the photonic crystal fiber and the polarization-maintaining single-mode fiber. Using the far-field measurement results from the fabricated samples, we show that the waveguide loss to be ~0.3dB/μm, which agrees closely with the simulated loss of ~ 0.28 dB/μm for the fundamental mode of plasmonic slot waveguide. Since all these multiple channels are excited from the input light of the fiber's core, we further expand the functionalization and develop selective excitation/switching devices. We further developed polarization-switching element that consists of four different waveguides where one pair can be excited with horizontal incident polarization from the core and another pair can be excited by vertical polarization. Finally, the selective excitation element is further extended to wavelength-dependent optical switch where the output signals from two output ports can be selectively excited depending on the incident wavelength of the light from the core. This led to a functional nanoscale optical directional coupler on optical fibers and optical switching is observed while scanning the wavelength from 1480 nm to 1650 nm.

Next, the works of incorporating metasurface on the optical fiber involved in making two major devices- in-fiber color filter and metalens in single-mode fiber. A polarization-dependent color filtering effect is demonstrated by fabricating asymmetric cross holes in the photonic crystal fiber and single-mode fiber that shows transmission peaks at the telecommunication wavelength ranges and are in good agreement with the simulation results. Also, another type of metasurface, namely, geometric phase antenna is fabricated on the facet of a single-mode fiber. Far-field measurements demonstrate a focusing effect is observed at 32 microns from the end-face of the optical fiber. This work is in conjunction with and later resulted in designing the metalens in photonic crystal fiber.

Another work involves a temperature dependence phase transition of vanadium dioxide (VO_2). Here, we have studied the optical modulation by incorporating the VO_2 nanocrystals into the airy holes of anti-resonant hollow-core photonic crystal fibers. The study shows that the polarization-independent modulation bandwidth can be achieved that encompasses the S+C+L band.

In conclusion, a detailed study on the integration of metasurfaces, plasmonic nano-circuits in the facet of optical fibers together with the insertion of VO_2 nanocrystals has been presented in this dissertation. This works can find applications in various areas for modifying optical properties of optical fibers, in-fiber optical imaging, optical sensing, and medical endoscopy. The integration of plasmonic nanocircuits in the optical fiber can provide a completely different chip-scale communication system on optical fiber where the functionally integrated chip is directly coupled and functionalized on the end face of the optical fibers.

BIBLIOGRAPHY

1. Kao KC, Hockham GA, editors. Dielectric-fiber surface waveguides for optical frequencies. Proceedings of the Institution of Electrical Engineers; 1966: IET.

2. Russell PSJ. Photonic-Crystal Fibers. J Lightwave Technol. 2006;24(12):4729-49.

3. Chowdhury S, Sen S, Ahmed K, Asaduzzaman S. Design of highly sensible porous shaped photonic crystal fiber with strong confinement field for optical sensing. Optik. 2017;142:541-9.

4. Ademgil H, Haxha S. Highly birefringent nonlinear PCF for optical sensing of analytes in aqueous solutions. Optik. 2016;127(16):6653-60.

5. Birks T, Wadsworth W, Russell PSJ. Supercontinuum generation in tapered fibers. Optics letters. 2000;25(19):1415-7.

6. Kumar VRK, George A, Reeves W, Knight J, Russell PSJ, Omenetto F, et al. Extruded soft glass photonic crystal fiber for ultrabroad supercontinuum generation. Optics Express. 2002;10(25):1520-5.

7. Leon-Saval S, Birks T, Wadsworth W, Russell PSJ, Mason M. Supercontinuum generation in submicron fibre waveguides. Optics Express. 2004;12(13):2864-9.

8. Chang W, Nazarkin A, Travers J, Nold J, Hölzer P, Joly N, et al. Influence of ionization on ultrafast gas-based nonlinear fiber optics. Optics express. 2011;19(21):21018-27.

9. Travers JC, Chang W, Nold J, Joly NY, Russell PSJ. Ultrafast nonlinear optics in gas-filled hollow-core photonic crystal fibers. JOSA B. 2011;28(12):A11-A26.

10. Tseng M-Y, Lin J-C, Huang T-Y, Shih Y-L, Chu H-C, Chang W-K, et al. Endoscopic submucosal dissection for early colorectal neoplasms: clinical experience in a tertiary medical center in taiwan. Gastroenterology research and practice. 2013;2013.

11. Patel MR, Shah RN, Snyderman CH, Carrau RL, Germanwala AV, Kassam AB, et al. Pericranial flap for endoscopic anterior skull-base reconstruction: clinical outcomes and radioanatomic analysis of preoperative planning. Neurosurgery. 2010;66(3):506-12.

12. Brongersma ML, Shalaev VM. The case for plasmonics. science. 2010;328(5977):440-1.

13. Aieta F, Genevet P, Kats MA, Yu NF, Blanchard R, Gahurro Z, et al. Aberration-Free Ultrathin Flat Lenses and Axicons at Telecom Wavelengths Based on Plasmonic Metasurfaces. Nano Lett. 2012;12(9):4932-6.

14. Kang M, Feng TH, Wang HT, Li JS. Wave front engineering from an array of thin aperture antennas. Opt Express. 2012;20(14):15882-90.

15. Genevet P, Yu NF, Aieta F, Lin J, Kats MA, Blanchard R, et al. Ultra-thin plasmonic optical vortex plate based on phase discontinuities. Appl Phys Lett. 2012;100(1):013101.

16. Chen WT, Yang K-Y, Wang C-M, Huang Y-W, Sun G, Chiang I-D, et al. High-Efficiency Broadband Meta-Hologram with Polarization-Controlled Dual Images. Nano Lett. 2014;14(1):225-30.

17. Ni XJ, Kildishev AV, Shalaev VM. Metasurface holograms for visible light. Nat Commun. 2013;4:2807.

18. Zheng G, Muhlenbernd H, Kenney M, Li G, Zentgraf T, Zhang S. Metasurface holograms reaching 80% efficiency. Nature Nanotechnology. 2015;10:308-12.

19. Genevet P, Capasso F. Holographic optical metasurfaces: a review of current progress. Reports on Progress in Physics. 2015;78(2):024401.

20. Huang L, Chen X, Muhlenbernd H, Zhang H, Chen S, Bai B, et al. Three-dimensional optical holography using a plasmonic metasurface. Nat Commun. 2013;4:2808.

21. Lin J, Mueller JPB, Wang Q, Yuan GH, Antoniou N, Yuan XC, et al. Polarization-Controlled Tunable Directional Coupling of Surface Plasmon Polaritons. Science. 2013;340(6130):331-4.

22. Jin J, Luo J, Zhang X, Gao H, Li X, Pu M, et al. Generation and detection of orbital angular momentum via metasurface. Sci Rep. 2016;6:24286

23. Li G, Kang M, Chen S, Zhang S, Pun EY-B, Cheah KW, et al. Spin-Enabled Plasmonic Metasurfaces for Manipulating Orbital Angular Momentum of Light. Nano Lett. 2013;13:4148–51.

24. Karimi E, Schulz SA, Leon ID, Qassim H, Upham J, Boyd RW. Generating optical orbital angular momentum at visible wavelengths using a plasmonic metasurface. Light: Science & Applications. 2014;3:e167.

25. Huang KC, Seo M-K, Sarmiento T, Huo Y, Harris JS, Brongersma ML. Electrically driven subwavelength optical nanocircuits. Nature Photonics. 2014;8(3):244-9.

26. Gramotnev DK, Bozhevolnyi SI. Plasmonics beyond the diffraction limit. Nature photonics. 2010;4(2):83-91.

27. Veronis G, Fan S. Modes of subwavelength plasmonic slot waveguides. J Lightwave Technol. 2007;25(9):2511-21.

28. Wen J, Banzer P, Kriesch A, Ploss D, Schmauss B, Peschel U. Experimental cross-polarization detection of coupling far-field light to highly confined plasmonic gap modes via nanoantennas. Applied Physics Letters. 2011;98(10):101109.

29. Geisler P, Razinskas G, Krauss E, Wu X-F, Rewitz C, Tuchscherer P, et al. Multimode plasmon excitation and in situ analysis in top-down fabricated nanocircuits. Physical review letters. 2013;111(18):183901.

30. Naghizadeh S, Afridi A, Arısev O, Karaşahin A, Kocabaş ŞE. Experimental investigation of stub resonators built in plasmonic slot waveguides. IEEE Photonics Technology Letters. 2017;29(8):663-6.

31. Ly-Gagnon D-S, Balram KC, White JS, Wahl P, Brongersma ML, Miller DA. Routing and photodetection in subwavelength plasmonic slot waveguides. Nanophotonics. 2012;1(1):9-16.

32. Kriesch A, Burgos SP, Ploss D, Pfeifer H, Atwater HA, Peschel U. Functional Plasmonic Nanocircuits with Low Insertion and Propagation Losses. Nano Letters. 2013;13(9):4539-45.

33. No Y-S, Choi J-H, Ee H-S, Hwang M-S, Jeong K-Y, Lee E-K, et al. A double-strip plasmonic waveguide coupled to an electrically driven nanowire LED. Nano letters. 2013;13(2):772-6.

34. Gao Q, Ren F, Wang AX. Direct and efficient optical coupling into plasmonic integrated circuits from optical fibers. IEEE Photonics Technology Letters. 2016;28(11):1165-8.

35. Aihara T, Sakai H, Takeda A, Okahisa S, Fukuhara M, Ota M, et al. Coherent plasmonic interconnection in silicon-based electrical circuit. J Lightwave Technol. 2015;33(10):2139-45.

36. Ropers C, Neacsu C, Elsaesser T, Albrecht M, Raschke M, Lienau C. Grating-coupling of surface plasmons onto metallic tips: a nanoconfined light source. Nano letters. 2007;7(9):2784-8.

37. Feigenbaum E, Orenstein M. Backward propagating slow light in inverted plasmonic taper. Optics express. 2009;17(4):2465-9.

38. Song Y, Wang J, Li Q, Yan M, Qiu M. Broadband coupler between silicon waveguide and hybrid plasmonic waveguide. Optics express. 2010;18(12):13173-9.

39. Zhang S, Gu C, Xu H. Single nanoparticle couplers for plasmonic waveguides. Small. 2014;10(21):4264-9.

40. Obelleiro F, Taboada J, Solís D, Bote L. Directive antenna nanocoupler to plasmonic gap waveguides. Optics letters. 2013;38(10):1630-2.

41. Andryieuski A, Zenin VA, Malureanu R, Volkov VS, Bozhevolnyi SI, Lavrinenko AV. Direct characterization of plasmonic slot waveguides and nanocouplers. Nano letters. 2014;14(7):3925-9.

42. Huang J-S, Feichtner T, Biagioni P, Hecht B. Impedance matching and emission properties of nanoantennas in an optical nanocircuit. Nano letters. 2009;9(5):1897-902.

43. Balanis CA. Antenna theory: analysis and design: John wiley & sons; 2016.

44. Andryieuski A, Malureanu R, Bouillard J-S, Zayats AV, Lavrinenko AV, editors. Improving plasmonic waveguides coupling efficiency using nanoantennas. 2012 14th International Conference on Transparent Optical Networks (ICTON); 2012: IEEE.

45. Tao J, Hu B, He XY, Wang QJ. Tunable subwavelength terahertz plasmonic stub waveguide filters. IEEE transactions on nanotechnology. 2013;12(6):1191-7.

46. Burgos SP, Lee HW, Feigenbaum E, Briggs RM, Atwater HA. Synthesis and characterization of plasmonic resonant guided wave networks. Nano letters. 2014;14(6):3284-92.

47. Lee HW, Papadakis G, Burgos SP, Chander K, Kriesch A, Pala R, et al. Nanoscale conducting oxide PlasMOStor. Nano letters. 2014;14(11):6463-8.

48. Winzer PJ, Neilson DT, Chraplyvy AR. Fiber-optic transmission and networking: the previous 20 and the next 20 years [Invited]. Opt Express. 2018;26(18):24190-239.

49. Dragic PD, Cavillon M, Ballato J. Materials for optical fiber lasers: A review. Appl Phys Rev. 2018;5:041301.

50. Urrutia A, Villar ID, Zubiate P, Zamarreño CR. A Comprehensive Review of Optical Fiber Refractometers: Toward a Standard Comparative Criterion. Laser & Photonics Reviews. 2019;13:1900094.

51. Lee HK, Choo J, Kim J. Multiplexed Passive Optical Fiber Sensor Networks for Water Level Monitoring: A Review. Sensors (Basel). 2020;20(23).

52. Orth A, Ploschner M, Wilson ER, Maksymov IS, Gibson BC. Optical fiber bundles: Ultra-slim light field imaging probes. Sci Adv. 2019;5(4):eaav1555.

53. Socorro-Leránoz AB, Santano D, Villar ID, Matias IR. Trends in the design of wavelength-based optical fibre biosensors. Biosensors and Bioelectronics: X. 2019;1:100015.

54. Čižmár T, Dholakia K. Shaping the light transmission through a multimode optical fibre: complex transformation analysis and applications in biophotonics. Opt Express. 2011;19:18871-84.

55. Ioannis N. Papadopoulos SF, Christophe Moser, and Demetri Psaltis. High-resolution, lensless endoscope based on digital scanning through a multimode optical fiber. Optical Society of America. 2013.

56. Liang Y, Yu Z, Li L, Xu T. A self-assembled plasmonic optical fiber nanoprobe for label-free biosensing. Sci Rep. 2019;9(1):7379.

57. Jia P, Yang J. Integration of large-area metallic nanohole arrays with multimode optical fibers for surface plasmon resonance sensing. Applied Physics Letters. 2013;102(24).

58. Nguyen H, Sidiroglou F, Collins SF, Davis TJ, Roberts A, Baxter GW. A localized surface plasmon resonance-based optical fiber sensor with sub-wavelength apertures. Applied Physics Letters. 2013;103(19).

59. Feng S, Darmawi S, Henning T, Klar PJ, Zhang X. A miniaturized sensor consisting of concentric metallic nanorings on the end facet of an optical fiber. Small. 2012;8(12):1937-44.

60. Wang N, Zeisberger M, Hübner U, Schmidt MA. Nanotrimer enhanced optical fiber tips implemented by electron beam lithography. Optical Materials Express. 2018;8:2246-55.

61. Yang J, Ghimire I, Wu PC, Gurung S, Arndt C, Tsai DP, et al. Photonic crystal fiber metalens. Nanophotonics. 2019;8(3):443-9.

62. Savinov V, Zheludev NI. High-quality metamaterial dispersive grating on the facet of an optical fiber. Applied Physics Letters. 2017;111(9).

63. Arabi HE, Joe HE, Nazari T, Min BK, Oh K. A high throughput supra-wavelength plasmonic bull's eye photon sorter spatially and spectrally multiplexed on silica optical fiber facet. Opt Express. 2013;21(23):28083-94.

64. Principe M, Consales M, Micco A, Crescitelli A, Castaldi G, Esposito E, et al. Optical fiber meta-tips. Light Sci Appl. 2017;6(3):e16226.

65. Kang S, Joe H-E, Kim J, Jeong Y, Min B-K, Oh K. Subwavelength plasmonic lens patterned on a composite optical fiber facet for quasi-one-dimensional Bessel beam generation. Applied Physics Letters. 2011;98(24).

66. Yermakov O, Schneidewind H, Hübner U, Wieduwilt T, Zeisberger M, Bogdanov A, et al. Nanostructure-Empowered Efficient Coupling of Light into Optical Fibers at Extraordinarily Large Angles. Acs Photonics. 2020;7:2834-41.

67. Wang N, Zeisberger M, Hübner U, Schmidt MA. Boosting Light Collection Efficiency of Optical Fibers Using Metallic Nanostructures. Acs Photonics. 2019;6:691-8.

68. Yang X, Ileri N, Larson CC, Carlson TC, Britten JA, Chang AS, et al. Nanopillar array on a fiber facet for highly sensitive surface-enhanced Raman scattering. Opt Express. 2012;20(22):24819-26.

69. Jeong HH, Erdene N, Park JH, Jeong DH, Lee HY, Lee SK. Real-time label-free immunoassay of interferon-gamma and prostate-specific antigen using a Fiber-Optic Localized Surface Plasmon Resonance sensor. Biosens Bioelectron. 2013;39(1):346-51.

70. Kostovski G, Chinnasamy U, Jayawardhana S, Stoddart PR, Mitchell A. Sub-15nm optical fiber nanoimprint lithography: A parallel, self-aligned and portable approach. Adv Mater. 2011;23(4):531-5.

71. Lipomi DJ, Martinez RV, Kats MA, Kang SH, Kim P, Aizenberg J, et al. Patterning the tips of optical fibers with metallic nanostructures using nanoskiving. Nano Lett. 2011;11(2):632-6.

72. Shambata) G, Provine J, Rivoire K, Sarmiento T, Harris J, Vučković J. Optical fiber tips functionalized with semiconductor photonic crystal cavities. Appl Phys Lett. 2011;99:191102.

73. Reader-Harris P, Di Falco A. Nanoplasmonic Filters for Hollow Core Photonic Crystal Fibers. Acs Photonics. 2014;1(10):985-9.

74. Chong A, Buckley J, Renninger W, Wise F. All-normal-dispersion femtosecond fiber laser. Optics express. 2006;14(21):10095-100.

75. Jeong Ye, Sahu J, Payne Da, Nilsson J. Ytterbium-doped large-core fiber laser with 1.36 kW continuous-wave output power. Optics express. 2004;12(25):6088-92.

76. Papadopoulos IN, Farahi S, Moser C, Psaltis D. High-resolution, lensless endoscope based on digital scanning through a multimode optical fiber. Biomedical optics express. 2013;4(2):260-70.

77. Katoot MW. Optical fiber imaging system. Google Patents; 2000.

78. Nathaniel M, Fried M, Murray K. High-power thulium fiber laser ablation of urinary tissues at 1.94 μm. Journal of Endourology. 2005;19:25-31.

79. Alster TS, Tanzi EL, Lazarus M. The use of fractional laser photothermolysis for the treatment of atrophic scars. Dermatologic Surgery. 2007;33(3):295-9.

80. Yin S, Ruffin P. Fiber optic sensors. Wiley Encyclopedia of Biomedical Engineering. 2006.

81. Hurot C, Ismail WZW, Dawes JM. Random laser in a fiber: combined effects of guiding and scattering lead to a reduction of the emission threshold. Optical Data Processing and Storage. 2017;3(1):97-100.

82. Chen WT, Zhu AY, Khorasaninejad M, Shi Z, Sanjeev V, Capasso F. Immersion meta-lenses at visible wavelengths for nanoscale imaging. Nano letters. 2017;17(5):3188-94.

83. Khorasaninejad M, Chen WT, Devlin RC, Oh J, Zhu AY, Capasso F. Metalenses at visible wavelengths: Diffraction-limited focusing and subwavelength resolution imaging. Science. 2016;352(6290):1190-4.

84. Khorasaninejad M, Chen W, Zhu A, Oh J, Devlin R, Rousso D, et al. Multispectral chiral imaging with a metalens. Nano letters. 2016;16(7):4595-600.

85. Wu PC, Tsai W-Y, Chen WT, Huang Y-W, Chen T-Y, Chen J-W, et al. Versatile polarization generation with an aluminum plasmonic metasurface. Nano letters. 2017;17(1):445-52.

86. Pu M, Li X, Ma X, Wang Y, Zhao Z, Wang C, et al. Catenary optics for achromatic generation of perfect optical angular momentum. Science Advances. 2015;1(9):e1500396.

87. Zheng G, Mühlenbernd H, Kenney M, Li G, Zentgraf T, Zhang S. Metasurface holograms reaching 80% efficiency. Nature nanotechnology. 2015;10(4):308-12.

88. Li X, Chen L, Li Y, Zhang X, Pu M, Zhao Z, et al. Multicolor 3D meta-holography by broadband plasmonic modulation. Science advances. 2016;2(11):e1601102.

89. Ye W, Zeuner F, Li X, Reineke B, He S, Qiu C-W, et al. Spin and wavelength multiplexed nonlinear metasurface holography. Nature communications. 2016;7(1):1-7.

90. Chen WT, Zhu AY, Sanjeev V, Khorasaninejad M, Shi Z, Lee E, et al. A broadband achromatic metalens for focusing and imaging in the visible. Nature nanotechnology. 2018;13(3):220-6.

91. Kim H, An H, Kim J, Lee S, Park K, Lee S, et al. Corrugation-assisted metal-coated angled fiber facet for wavelength-dependent off-axis directional beaming. Optics express. 2017;25(7):8366-85.

92. Savinov V, Zheludev NI. High-quality metamaterial dispersive grating on the facet of an optical fiber. Applied Physics Letters. 2017;111(9):091106.

93. Saleh AA, Sheikhoelislami S, Gastelum S, Dionne JA. Grating-flanked plasmonic coaxial apertures for efficient fiber optical tweezers. Optics express. 2016;24(18):20593-603.

94. Wang N, Zeisberger M, Hübner U, Schmidt MA. Nanotrimer enhanced optical fiber tips implemented by electron beam lithography. Optical Materials Express. 2018;8(8):2246-55.

95. Zhang Z, Chen Y, Liu H, Bae H, Olson DA, Gupta AK, et al. On-fiber plasmonic interferometer for multi-parameter sensing. Optics express. 2015;23(8):10732-40.

96. Jia P, Yang J. Integration of large-area metallic nanohole arrays with multimode optical fibers for surface plasmon resonance sensing. Applied Physics Letters. 2013;102(24):243107.

97. Pahlevaninezhad H, Khorasaninejad M, Huang Y-W, Shi Z, Hariri LP, Adams DC, et al. Nano-optic endoscope for high-resolution optical coherence tomography in vivo. Nature photonics. 2018;12(9):540-7.

98. Lee HWH, Yang J, Ghimire I. Metasurface on optical fiber and related method. Google Patents; 2020.

99. Cormier P, Son TV, Thibodeau J, Doucet A, Truong V-V, Haché A. Vanadium dioxide as a material to control light polarization in the visible and near infrared. Optics Communications. 2017;382:80-5.

100. Kim Y, Wu PC, Sokhoyan R, Mauser K, Glaudell R, Kafaie Shirmanesh G, et al. Phase modulation with electrically tunable vanadium dioxide phase-change metasurfaces. Nano Letters. 2019;19(6):3961-8.

101. Lei L, Lou F, Tao K, Huang H, Cheng X, Xu P. Tunable and scalable broadband metamaterial absorber involving VO 2-based phase transition. Photonics Research. 2019;7(7):734-41.

102. Prayakarao S, Mendoza B, Devine A, Kyaw C, Van Dover R, Liberman V, et al. Tunable VO2/Au hyperbolic metamaterial. Applied Physics Letters. 2016;109(6):061105.

103. Dicken MJ, Aydin K, Pryce IM, Sweatlock LA, Boyd EM, Walavalkar S, et al. Frequency tunable near-infrared metamaterials based on VO 2 phase transition. Optics express. 2009;17(20):18330-9.

104. Aydin K, Ferry VE, Briggs RM, Atwater HA. Broadband polarization-independent resonant light absorption using ultrathin plasmonic super absorbers. Nature communications. 2011;2(1):1-7.

105. Rahimi E, Şendur K. Temperature-driven switchable-beam Yagi-Uda antenna using VO2 semiconductor-metal phase transitions. Optics Communications. 2017;392:109-13.

106. Prasad A, Amirthapandian S, Dhara S, Dash S, Murali N, Tyagi A. Novel single-phase vanadium dioxide nanostructured films for methane sensing near room temperature. Sensors and Actuators B: Chemical. 2014;191:252-6.

107. Qazilbash MM, Brehm M, Chae B-G, Ho P-C, Andreev GO, Kim B-J, et al. Mott transition in VO2 revealed by infrared spectroscopy and nano-imaging. Science. 2007;318(5857):1750-3.

108. Horrocks GA, Singh S, Likely MF, Sambandamurthy G, Banerjee S. Scalable hydrothermal synthesis of free-standing VO2 nanowires in the M1 phase. ACS applied materials & interfaces. 2014;6(18):15726-32.

109. Andrews JL, Santos DA, Meyyappan M, Williams RS, Banerjee S. Building brain-inspired logic circuits from dynamically switchable transition-metal oxides. Trends in Chemistry. 2019;1(8):711-26.

110. Currie M, Mastro MA, Wheeler VD. Characterizing the tunable refractive index of vanadium dioxide. Optical Materials Express. 2017;7(5):1697-707.

111. Kim JT. CMOS-compatible hybrid plasmonic modulator based on vanadium dioxide insulator-metal phase transition. Optics letters. 2014;39(13):3997-4000.

112. Shibuya K, Atsumi Y, Yoshida T, Sakakibara Y, Mori M, Sawa A. Silicon waveguide optical modulator driven by metal–insulator transition of vanadium dioxide cladding layer. Optics express. 2019;27(4):4147-56.

113. Sánchez L, Lechago S, Sanchis P. Ultra-compact TE and TM pass polarizers based on vanadium dioxide on silicon. Optics letters. 2015;40(7):1452-5.

114. Lei DY, Appavoo K, Ligmajer F, Sonnefraud Y, Haglund Jr RF, Maier SA. Optically-triggered nanoscale memory effect in a hybrid plasmonic-phase changing nanostructure. ACS photonics. 2015;2(9):1306-13.

115. Matjasec Z, Campelj S, Donlagic D. All-optical, thermo-optical path length modulation based on the vanadium-doped fibers. Optics express. 2013;21(10):11794-807.

116. Preložnik B, Gleich D, Donlagic D. All-fiber, thermo-optic liquid level sensor. Optics express. 2018;26(18):23518-33.

117. Ding W, Wang Y-Y, Gao S-F, Wang M-L, Wang P. Recent progress in low-loss hollow-core anti-resonant fibers and their applications. IEEE Journal of Selected Topics in Quantum Electronics. 2019;26(4):1-12.

118. Gao S-F, Wang Y-Y, Liu X-L, Ding W, Wang P. Bending loss characterization in nodeless hollow-core anti-resonant fiber. Optics express. 2016;24(13):14801-11.

119. Wang Y, Ding W. Confinement loss in hollow-core negative curvature fiber: A multi-layered model. Optics Express. 2017;25(26):33122-33.

120. Gao S-f, Wang Y-y, Ding W, Jiang D-l, Gu S, Zhang X, et al. Hollow-core conjoined-tube negative-curvature fibre with ultralow loss. Nature communications. 2018;9(1):1-6.

121. Fleer NA, Pelcher KE, Zou J, Nieto K, Douglas LD, Sellers DG, et al. Hybrid nanocomposite films comprising dispersed VO2 nanocrystals: a scalable aqueous-phase route to thermochromic fenestration. ACS applied materials & interfaces. 2017;9(44):38887-900.

122. Fleer NA, Pelcher KE, Nieto K, Braham EJ, Zou J, Horrocks GA, et al. Elucidating the Crystallite Size Dependence of the Thermochromic Properties of Nanocomposite VO2 Thin Films. ACS omega. 2018;3(10):14280-93.

123. Kana JK, Ndjaka J, Vignaud G, Gibaud A, Maaza M. Thermally tunable optical constants of vanadium dioxide thin films measured by spectroscopic ellipsometry. Optics Communications. 2011;284(3):807-12.

124. Tadjer MJ, Wheeler VD, Downey BP, Robinson ZR, Meyer DJ, Eddy Jr CR, et al. Temperature and electric field induced metal-insulator transition in atomic layer deposited VO2 thin films. Solid-State Electronics. 2017;136:30-5.

125. Chang Z, Chiang KS. Experimental verification of optical models of graphene with multimode slab waveguides. Optics letters. 2016;41(9):2129-32.

126. Lee H, Schmidt M, Russell PSJ. Excitation of a nanowire "molecule" in gold-filled photonic crystal fiber. Optics letters. 2012;37(14):2946-8.

127. Whittaker L, Patridge CJ, Banerjee S. Microscopic and nanoscale perspective of the metal− insulator phase transitions of VO2: some new twists to an old tale. The Journal of Physical Chemistry Letters. 2011;2(7):745-58.

128. Shao Z, Cao X, Luo H, Jin P. NPG Asia Mater. 10, 581 (2018).

129. Jager MF, Ott C, Kraus PM, Kaplan CJ, Pouse W, Marvel RE, et al. Tracking the insulator-to-metal phase transition in VO2 with few-femtosecond extreme UV transient absorption spectroscopy. Proceedings of the National Academy of Sciences. 2017;114(36):9558-63.